Intrinsic Fracture Toughness of a Soft Viscoelastic Adhesive

Xingwei Yang[1], Michael J. Wald[2], Ryan Birringer[2], Jonathan Kemling[2], Aaron Hedegaard[2], John Martin[2], Jason Clapper[3], Rong Long[1*]

[1]Paul M. Rady Department of Mechanical Engineering, University of Colorado Boulder, Boulder, CO 80309, USA.

[2]Corporate Research Analytical Laboratory, 3M Company, St. Paul, MN 55144, USA.

[3]Corporate Research Materials Laboratory, 3M Company, St. Paul, MN 55144, USA.

*Corresponding author: rong.long@colorado.edu

Abstract

The fracture toughness of inelastic materials consists of an intrinsic component associated with the crack tip fracture process and a dissipative component due to bulk dissipation. Experimental characterization of the intrinsic component of fracture toughness is important for understanding the fracture mechanism and predictive modeling of the fracture behavior. Here we present an experimental study on the intrinsic toughness of a soft viscoelastic adhesive. We first obtained full-field and full-history data of the displacement and deformation fields in pure shear fracture tests using a particle tracking method. By combining these data with a nonlinear constitutive model, we extracted the intrinsic toughness through an energy balance analysis. A two-stage crack propagation behavior was observed in our fracture experiments: under monotonic loading the crack first underwent a slow propagation stage and then suddenly entered a fast propagation stage. We found that the intrinsic toughness was highly scattered for the slow propagation stage, but remained consistent for the fast propagation stage. Further examination of the fracture surface and the onset of fast propagation revealed that transition from the slow to the fast propagation stage was governed by the applied stretch and was likely due to a change in the crack tip fracture process.

Keywords

Fracture toughness, crack propagation, viscoelasticity, pressure sensitive adhesives, particle tracking.

1. Introduction

The fracture toughness of viscoelastic solids is known to be dependent on the velocity of crack propagation (Gent, 1996; Knauss, 2015). This behavior, widely observed in elastomers (Knauss, 1973), rubber (Greensmith, 1964; Tsunoda et al., 2000) and soft adhesives (Creton and Ciccotti, 2016), has sparked long-lasting interests in understanding the underlying physical mechanism (Hui et al., 2022). In particular, the fracture toughness of polyurethane elastomer and synthetic rubber measured at different loading rates and temperatures was found to follow the time-temperature superposition principle (Knauss, 2015), implying the central role played by viscoelasticity. A number of theoretical models have been developed to capture the effect of viscoelasticity on crack propagation (Knauss, 1973; Schapery, 1975a; Hui et al., 1992; de Gennes, 1996; Greenwood, 2004; Persson and Brener, 2005). These models, typically assuming steady-state crack propagation in a linear viscoelastic solid, can be categorized into two approaches. In both approaches, the moving crack tip is assumed to be subjected to an asymptotic stress field following the *K*-field in linear elastic fracture mechanics (Persson and Brener, 2005; Knauss, 2015). This assumption, which can be justified using the extended correspondence principle of linear viscoelasticity (Graham, 1968), allows one to specify the crack tip stress field by prescribing the stress intensity factor *K*. After this common assumption, the two approaches depart from each other.

In the first approach (Knauss, 1973; Schapery, 1975a, 1975b, 1975c; Greenwood, 2004; Knauss, 2015), the crack tip fracture process is modeled by a cohesive zone, within which the crack opening displacement is solved using the prescribed stress intensity factor *K* and the linear viscoelastic constitutive relation. Since the crack is under steady-state propagation, the opening displacement in the cohesive zone depends on the crack velocity and satisfies a fracture criterion, resulting in an equation relating the crack velocity to the prescribed stress intensity factor *K*. The second approach takes an energetic perspective and focuses on calculating the viscoelastic energy dissipation around the moving crack tip (de Gennes, 1996; Saulnier et al., 2004; Persson and Brener, 2005). Rate-dependence of fracture toughness originates from the dependence of bulk viscoelastic dissipation on crack velocity. It was recently shown that these two approaches are qualitatively equivalent (Ciavarella et al., 2021; Hui et al., 2022) and can be represented by the following equation:

$$\Gamma = \Gamma_0 + \Gamma_D, \tag{1}$$

where Γ is the total energy required to propagate the crack by a unit area, Γ_0 is the intrinsic component of Γ that is associated with the crack tip fracture process, and Γ_D is the dissipative component representing the contribution due to bulk dissipation. More broadly, the decomposition in eq. (1) can be extended to polymeric materials with other types of inelastic behaviors, such as hydrogels or elastomers with sacrificial bond breaking (Gong et al., 2003; Gong, 2010; Sun et al., 2012; Ducrot et al., 2014). Regardless of the physical nature of inelasticity, these material systems share a common toughening principle: the loading-unloading hysteresis locally occurring around a propagating crack can induce bulk energy dissipation and hence increase the total toughness Γ (Long and Hui, 2016; Qi et al., 2018). This principle has been exploited as a general strategy for enhancing the fracture toughness of hydrogels and elastomers (Zhao, 2014; Creton and Ciccotti, 2016).

In the theoretical picture reviewed above, the intrinsic fracture toughness Γ_0 is often assumed to be a material constant. For example, Lake and Thomas (1967) suggested that Γ_0 for crosslinked rubbery networks is the energy required to break a layer of polymer chains across a unit area of the fracture plane. This model gives an estimate of Γ_0 that is on the order of 10 to 100 J/m^2, and predicts that Γ_0 depends on the chain length and the molar density of chains. The prediction of Γ_0 is found to agree well with experimental measurements for unfilled rubber (Ahagon and Gent, 1975) and hydrogel networks with highly regular network structure (Akagi et al., 2013). However, this model assumes that chain scission is localized around the crack tip and occurs over one mesh size of the network (~ 10 nm), which may not be valid for all polymer networks in general. Indeed, Slootman et al. (2020) recently used mechanophores and confocal microscopy to map the scission of covalent bonds around the crack, and found that bond scission can occur in a delocalized manner over hundreds of micrometers away from the crack. This work provides experimental evidence for a far more complex physical picture underlying Γ_0. Theoretically, Yang et al. (2019) proposed that the length scale over which chain scission occurs depends on imperfection within the polymer network. In comparison to a perfect network, the crack tip region where chain scission occurs in an imperfect network can be much larger, thereby leading to toughness enhancement even though the dissipative component Γ_D is insignificant. Following this idea, there have been extensive research interests in engineering soft polymers or gels with high toughness and low hysteresis by designing the molecular network structure (Kim et al., 2021; Wang et al., 2021; Nian et al., 2022)

and incorporating microscopic (Lin et al., 2019b, 2019a) or even macroscopic structural features (Wang et al., 2019; Xiang et al., 2019; Li et al., 2020).

Given the complexity of physical mechanisms involved in Γ_0, it is challenging to theoretically predict Γ_0 for soft polymers, which makes experimental characterization especially important. For polymers with low hysteresis, Γ_0 can be directly measured using fracture tests (Creton and Ciccotti, 2016) since Γ_D is small and thus $\Gamma_0 \approx \Gamma$. However, many soft polymers in engineering applications are designed to be highly dissipative (e.g., filled rubber and soft adhesives). For these dissipative materials, measurement of Γ_0 can be difficult due to the challenges in experimentally separating Γ_0 and Γ_D from the total fracture toughness Γ. It is worth mentioning that Zhang et al. (2015) demonstrated that for a tough hydrogel with interpenetrating polyacrylamide-alginate network, Γ_0 can be measured by pre-stretching the specimen to consume the dissipation mechanism and hence minimize Γ_D. Alternatively, when studying fracture of a carbon-black filled rubber, Roucou et al. (2020) first estimated Γ_D by measuring the peak deformation experienced by material points around the crack tip and then determined Γ_0 by subtracting Γ_D from Γ. In both works, the dominating dissipation mechanism is the stretch-induced softening, i.e., the Mullins effect (Diani et al., 2009), which is insensitive to crack velocity or loading rate. In contrast, bulk dissipation in viscoelastic solids is rate-dependent. As a result, pre-stretching or measuring the peak deformation is no longer sufficient for experimentally determining Γ_D in viscoelastic solids. Furthermore, if the viscoelastic solid is soft, severe blunting of the crack tip is expected during crack propagation. Under such large deformation, linear viscoelasticity and the *K*-field, a concept from linear elastic fracture mechanics, may not be applicable anymore, thereby resulting in a lack of theoretical models for viscoelastic fracture with large deformation.

In this work, we apply a particle tracking method (Qi et al., 2019; Lu et al., 2021) to experimentally characterize Γ_0 for a soft viscoelastic adhesive known as the pressure sensitive adhesive (PSA). By tracking the displacements of randomly distributed tracer particles on pure-shear fracture specimens, we are able to measure the full history of two-dimensional deformation fields during crack propagation. The particle tracking method has been recently used to probe the crack tip process zone in a brittle hydrogel (Li et al., 2023) or to map the dissipation fields during crack propagation in a viscoelastic hydrogel (Qi et al., 2024). In this work, we combine the measured deformation fields with a calibrated visco-hyperelastic constitutive model to enable the

computation of stress fields. By feeding the deformation and stress fields into a mechanical energy balance theory, we are able to circumvent Γ_D or Γ and directly determine Γ_0. This paper is organized as follows. The experimental methodology is described in Section 2, and representative results from the particle tracking method are shown in Section 3. In Section 4, we present the theoretical basis for extracting the intrinsic toughness Γ_0 and the associated experimental data. In Section 5, we present additional findings to explain the crack propagation behaviors observed in our experiments. We conclude in Section 6 by summarizing the main findings and outlining potential extension of our experimental method.

2. Materials and Methods

2.1 Pressure sensitive adhesive films

The PSA was generated by polymerizing a composition of acrylic monomers between carrier release liners to create a transferable viscoelastic film of approximately 250 μm in thickness. 2-ethylhexyl acrylate (60 g), isobornyl acrylate (25 g), 2-hydroxyethyl acrylate (15 g), and hexanediol diacrylate (0.15 g) were combined with 1,2-diphenyl-2,2-dimethoxyethanone (0.25 g), and 1,4-bis (3-mercaptobutyryloxy) butane (0.01 g) until all components were sufficiently dissolved and mixed. The solution was coated between siliconized PET liners at a set gap of 250 μm using a notch bar coating apparatus. The construction was then UV cured from both sides of the composite with fluorescent bulbs having an irradiance output centered around 365 nm and a dose of approximately 1,640 mJ/cm^2.

Laminated sheets of PSA were created by first removing one of the carrier release liners from two sheets of the PSA. One of the sheets was placed on a flat surface with the exposed PSA surface facing up. The second sheet was aligned with the exposed PSA surface facing toward that of the first sheet. One of the edges of each sheet was aligned and a handheld roller (Polymag Tek, Inc., Rochester, NY, USA) was used to laminate the sheets together starting at the aligned edge and progressing across the sheet. Two additional individual sheets were added to the laminate to create a laminated sheet with a thickness of approximately 1 mm. Rectangular strips that are 12.7 mm wide by 25.4 mm long were cut from the laminated sheets for uniaxial tensile tests. Uniaxial tensile tests were performed using an MTS RF100 electromechanical load frame (MTS Corporation, Eden Prairie, MN, USA). Force was measured using a +/− 25N load cell. Strain in the loading direction

was measured independently of the load frame using an Aramis adjustable base digital image correlation (DIC) system (GOM, Braunschweig, Germany). The DIC system consisted of two 4MP cameras (Teledyne DALSA, Waterloo, ON, Canada) with 20 mm focal length lenses (Schneider Titanar B 20, Bad Kreuznach, Germany). A 350 mm × 260 mm × 260 mm measuring volume was used for strain measurements. The speckle pattern used for strain measurement was applied to the samples using a black permanent marker. Tests were run using a constant crosshead velocity of 10 mm/min, 100 mm/min, and 1000 mm/min. Each test was terminated when the tracking pattern moved out of the field of view of the DIC system. Five replicates were run for each crosshead velocity. The three crosshead velocities correspond to stretch rates (measured by DIC) of 0.0015 s^{-1}, 0.015 s^{-1} and 0.14 s^{-1}, respectively.

Viscoelastic property of the PSA was characterized as a function of temperature and oscillatory frequency using shear dynamic mechanical analysis (DMA). 8-mm diameter disk samples were punched from the laminated sheet. The release liners were removed from PSA, which was then mounted between two 8-mm diameter parallel plates attached to an ARES G2 strain controlled rotational rheometer (Waters/TA Instruments, New Castle, DE). Temperature of the sample and test plates was controlled using a nitrogen-purged forced convection oven, using liquid nitrogen for additional temperature control to sub-ambient conditions. Using this setup, glass transition temperature (T_g) of the PSA was measured to be −16.5 ºC using an oscillating strain (amplitude ≈ 1% and frequency = 1 Hz) with a temperature scan of 3 ºC per minute. For the characterization of viscoelasticity, the PSA was subjected to rotational oscillatory shear deformations at 100 °C at frequencies from 0.1 Hz to 10 Hz, with frequencies sampled logarithmically at 5 points per decade. The initial strain amplitude of this deformation was 5%, which could decrease as the PSA modulus increased, to maintain small strain conditions and satisfy assumptions of linear viscoelasticity. This frequency sweep measurement was then repeated on the same specimen in 5 °C increments, cooling down to a final temperature of −60 °C. The resulting frequency sweeps were then shifted according to the principles of time-temperature superposition (TTS), holding the 25 °C frequency sweep as the reference data set and shifting the results at the remaining temperatures along the log-frequency axis to achieve optimal superposition of the storage modulus (G') signal. Prior to frequency-axis shifting, a vertical shift inversely proportional to the absolute temperature was applied to the dynamic modulus data to account for entropic stresses common to polymeric systems exhibiting rubber-like elasticity.

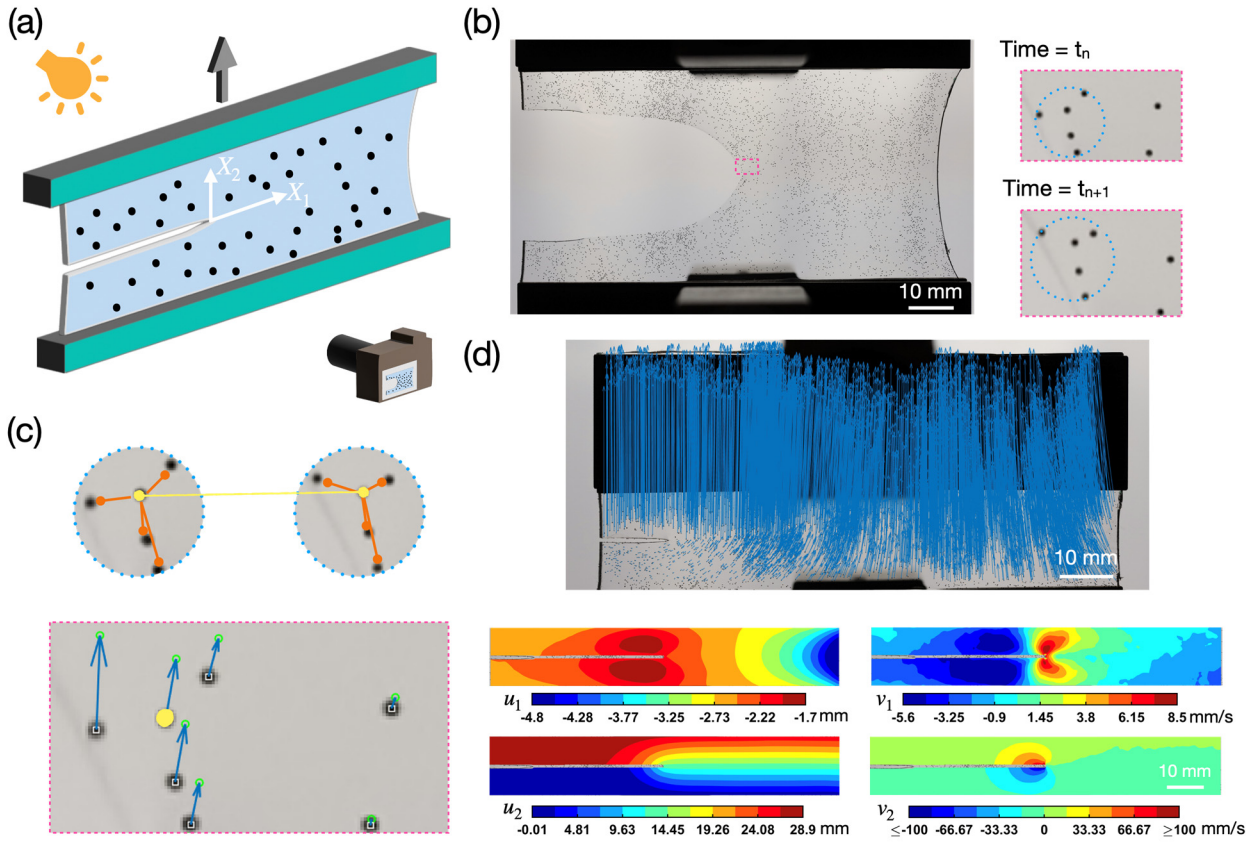

Figure 1 Crack propagation experiment with particle tracking. (a) Schematic of the pure shear fracture test geometry and the imaging setup. Origin of the coordinate system X_1-X_2 is located at the initial crack tip. (b) Representative image of the deformed sample (t = 2.88s) with insets showing a subset of tracer particles in two consecutive time frames (t_n = 2.88s and t_{n+1} = 2.89s) in an experiment with a loading rate of 0.5 s^{-1}. (c) Tracking particles between two consecutive time frames. Top: A representative pattern of neighboring particles around a tracked particle (highlighted in yellow). Bottom: Zoomed-in view of a region near the crack tip with tracer particle displacements (blue arrows) between two consecutive frames. (d) Top: Cumulative tracer particle displacements from the initial time frame (t = 0) to at t = 2.88s. Bottom: displacement fields (in-plane components u_1 and u_2) and velocity fields (in-plane components v_1 and v_2) at t = 2.88s.

2.2 Fracture experiments

Fracture experiments were conducted using the pure shear test geometry (Fig.1a). Thin-sheet fracture samples with dimensions of ~100 mm (width) × 70 mm (height) × ~ 1 mm (thickness) were cut from the laminated PSA sheets. An initial crack with a length of c_0 ~ 15 mm was introduced at the mid-height on one edge of each sample by a pair of scissors. We sprinkled black spherical glass beads (Cospheric LLC, Santa Barbara, CA) with diameters of 150~180 μm on the sample surface. These glass beads remained adhered to the sample surface during the entire

fracture experiment and hence can serve as tracer particles for mapping the two-dimensional (2D) deformation field on the sample surface. After that the sample was clamped by two sets of rigid plates and mounted on an Instron 5965 electromechanical load frame (Instron Corporation, Norwood, MA, USA), leaving a rectangular area of the sample (width L_0 ~ 100 mm and height H_0 ~ 20 mm) that underwent deformation during the fracture test. A pretension was applied before each test to leave a small initial crack opening of ~ 1 mm to prevent adhesion of the crack surfaces. A displacement Δ was applied to the upper boundary of the sample with a fixed loading rate $\dot{\Delta}/H_0$, while the bottom boundary of the sample remained fixed. The loading rate $\dot{\Delta}/H_0$ for different experiments was varied from 0.005 s^{-1} to 1 s^{-1}. During each fracture test, the sample was imaged using a digital camera (Canon EOS R5) with 4K resolution (i.e., 3840 pixels × 2160 pixels per image) and a frame rate of 120 frames per second. The camera was placed at a distance in front of the sample to achieve a spatial resolution of ~30 μm per pixel so that each tracer particle was captured by 5 ~ 6 pixels. To enhance the contrast between the tracer particles and the background, we used a white light source on the opposite side of the camera to illuminate the sample. Since the PSA samples were transparent, light emitted from the light source transmitted through the sample and was collected by the camera on the other side of the sample (Fig.1a).

2.3 Particle tracking method

We tracked the displacements of tracer particles using the images recorded from a fracture test. The procedures are briefly described here. First, the built-in function '*imfindcircles*' in MATLAB (MathWorks, Natick, MA, USA) was used to identify the tracer particles and obtain their centroid coordinates at each time frame of the recorded images (Fig.1b). Second, the Feature-Vector-Relaxation Method (FVRM) (Feng et al., 2014) was adopted to track the tracer particles in two consecutive frames. As shown in Fig.1c, this method leverages the relative positions of neighboring particles around a tracer particle as a geometrical signature for tracking. Specifically, the geometrical pattern formed by a target particle and its neighboring particles in the current image frame is compared with a few candidate patterns in the next image frame (Fig.1c). The pattern that best matches that in the current frame is selected, from which a pair of corresponding particles in the current and next frames is identified. Repeating this process for all tracer particles in the current image frame, we obtain the incremental tracer particle displacements between the current and the next image frame. By linking the incremental displacements for each tracer particle

from the first to the last image frame, one can determine the total displacements and trajectories of the tracer particles during an experiment.

2.4 Moving least square interpolation

The displacement data of tracer particles reflect the sample deformation upon loading and crack propagation. To quantify the 2D deformation field on the sample surface, we adopt the deformation gradient tensor **F** defined as:

$$\mathbf{F} = \nabla_{\mathbf{X}}\mathbf{u} + \boldsymbol{\delta}, \tag{2}$$

where **X** is the 2D coordinate vector of a material point in the initial time frame (i.e., the reference configuration for deformation; see Fig.1a), **u** is the displacement vector and **δ** is the identity tensor. The displacement field is represented by the function **u**(**X**). Evaluation of its spatial gradient requires us to interpolate the tracer particle displacements into a continuous field, which was achieved using the Moving Least Square (MLS) method (Liu and Long, 2016; Qi et al., 2019). To illustrate the principle of the MLS method, let us consider a generic scalar field function $f(\mathbf{X})$. Suppose its values are known at m points, i.e., $f(\mathbf{X} = \mathbf{d}_k) = w_k$ where $\mathbf{d}_k$ (k = 1, 2, ..., m) are coordinate vectors of the points and w_k are the corresponding values of $f(\mathbf{X})$. In this work, $\mathbf{d}_k$ represents the location of a tracer particle in the initial frame and w_k is the displacement component of the tracer particle. To determine the value of $f(\mathbf{X})$ at an arbitrary point **X**, we construct an interpolate function using a polynomial basis **P**(**X**) and the corresponding coefficients **a**(**X**) (both **P** and **a** are column vectors):

$$f(\mathbf{X}) = \mathbf{P}^{\mathrm{T}}(\mathbf{X})\mathbf{a}(\mathbf{X}). \tag{3}$$

Unlike conventional polynomial interpolation, the MLS method allows the coefficients **a** to be field functions as well, and thus can accommodate complex fields using relatively simple polynomial basis. For example, even the linear basis $\mathbf{P}(\mathbf{X}) = [1, X_1, X_2]^{\mathrm{T}}$ can capture a sophisticated field $f(\mathbf{X})$ due to the spatial variation in **a**(**X**). The coefficients **a**(**X**) are determined by minimizing a least-square error function:

$$L = \sum_{k=1}^{m} \zeta(\mathbf{X} - \mathbf{d}_k)\left[\mathbf{P}^{\mathrm{T}}(\mathbf{d}_k)\mathbf{a}(\mathbf{X}) - w_k\right]^2, \tag{4}$$

where $\zeta(\mathbf{X} - \mathbf{d}_k)$ is a weight function for the tracer beads that decays monotonically from 1 to 0 as the distance $|\mathbf{X} - \mathbf{d}_k|$ increases from 0 to $+\infty$. Following Qi et al.(2019), we adopted linear basis $\mathbf{P}(\mathbf{X}) = [1, X_1, X_2]^T$ and an exponential weight function:

$$\zeta(\mathbf{X} - \mathbf{d}_k) = \begin{cases} \dfrac{\exp\left(1 - \left|\mathbf{X} - \mathbf{d}_k\right|^2 / r_c^2\right) - 1}{\exp(1) - 1} & \left|\mathbf{X} - \mathbf{d}_k\right| \le r_c \\ 0 & \left|\mathbf{X} - \mathbf{d}_k\right| > r_c \end{cases}. \tag{5}$$

The cut-off radius r_c was chosen to be twice the average of the ten smallest values of $|\mathbf{X} - \mathbf{d}_k|$, i.e., twice the average distance to the ten closest tracer beads. As demonstrated by Qi et al.(2019), this set of MLS interpolation parameters can provide accurate measurement for the crack tip displacement and strain fields in soft elastomer. The MLS method described above was applied to the two displacement component: u_1 and u_2, thereby providing a continuous displacement field $\mathbf{u}(\mathbf{X})$.

An example of the tracer particle displacements and the interpolated displacement fields is shown in Fig.1d. The continuous fields of displacement components u_1 and u_2 establish a one-to-one mapping between the initial coordinates of any material point (i.e., X_1 and X_2) at $t = 0$ to its coordinates in the deformed configuration (i.e., $x_1 = X_1 + u_1$ and $x_2 = X_2 + u_2$) at any time frame t (> 0). Following the Lagrangian description of deformation, we use the initial coordinates (X_1, X_2) of a material point as its identifier, and thus will refer to the X_1-X_2 plane as the reference configuration. The displacement fields $u_1(X_1, X_2)$ and $u_2(X_1, X_2)$ at a representative time frame are shown in Fig.1d. Note that there is a non-colored strip (gap height $\approx$ 0.7 mm) in the contour map of u_1 and u_2. This strip represents the trajectory of crack propagation after being mapped to the reference configuration. The crack trajectory was obtained by first identifying the location of crack tip in the image of each time frame (i.e., the deformed configuration) and then mapping it back to the reference configuration using the interpolated displacement fields (Qi et al., 2019).

By interpolating the tracer particle displacements for all time frames, we obtained the full-field and full-history data of the displacement components u_1 and u_2. Spatial gradients of the displacement fields $u_1(X_1, X_2)$ and $u_2(X_1, X_2)$ result in the in-plane components of the deformation gradient tensor: F_{11}, F_{12}, F_{21} and F_{22} (see Eq. (2)), which will be illustrated in the next section. Time derivatives of u_1 and u_2 provide the velocity fields as shown in Fig.1d. Both spatial and

temporal variations of the displacement fields are needed for evaluating the stress fields in the PSA because of its viscoelastic nature.

2.5 Constitutive modeling

The deformation fields obtained from particle tracking allows us to further evaluate the stresses in the PSA samples during crack propagation. This step requires a nonlinear constitutive model capturing the viscoelastic behavior of the PSA. Although physics-based constitutive modeling is advantageous for capturing the nonlinear mechanical behaviors of soft elastomers (Vernerey et al., 2017), it is difficult for commercial PSAs which are often synthesized with complicated chemistry (e.g., see Section 2.1 for the chemical formulation of the PSA used in this work). Restrictions on the PSA chemistry originate from the need to achieve a compromise over the multi-faceted requirements for material properties, e.g., tackiness, low modulus, extensibility, high toughness and creep resistance (Creton, 2003). Additional requirements such as optical transparency, manufacturability and chemical stability may impose further constraints on the PSA chemistry. Therefore, we adopt a phenomenological model (Simo, 1987) for the PSAs used in this work. This model, schematically illustrated in the inset of Fig.2a, uses a hyperelastic model to accommodate large deformation and the Prony series to capture viscoelastic relaxation. Specifically, the Cauchy stress tensor $\boldsymbol{\sigma}$ is decomposed into a deviatoric component $\boldsymbol{\sigma}^D$ and a hydrostatic component $\sigma^H\boldsymbol{\delta}$ (recall that $\boldsymbol{\delta}$ is the identity tensor):

$$\boldsymbol{\sigma} = \boldsymbol{\sigma}^D + \sigma^H\boldsymbol{\delta}\,. \tag{6}$$

The deviatoric component $\boldsymbol{\sigma}^D$ at an arbitrary time t is given by a convolutional integral of the deformation history $\mathbf{F}(t)$ (Simo, 1987):

$$\boldsymbol{\sigma}^D(t) = \boldsymbol{\sigma}_0^D(t) + dev\left\{\mathbf{F}(t)\left[\int_0^t g'\left(t-t^*\right)\mathbf{F}^{-1}\left(t^*\right)\boldsymbol{\sigma}_0^D\left(t^*\right)\mathbf{F}^{-T}\left(t^*\right)dt^*\right]\mathbf{F}^T(t)\right\}, \tag{7}$$

where "*dev*" represents deviatoric component of a tensor, e.g., $dev(\mathbf{A}) = \mathbf{A} - [\mathrm{tr}(\mathbf{A})/3]\boldsymbol{\delta}$ for a generic tensor $\mathbf{A}$. In addition, $g' = dg/dt$ where $g(t)$ is a dimensionless relaxation function that decays 1 to 0 as t increases from 0, and $\boldsymbol{\sigma}_0^D(t)$ is the deviatoric stress due to the instantaneous elastic response which depends only on the current deformation gradient $\mathbf{F}(t)$ and is specified by a hyperelastic model. Note that Eq. (7) assumes that deformation starts at time $t = 0$ without loss of generality.

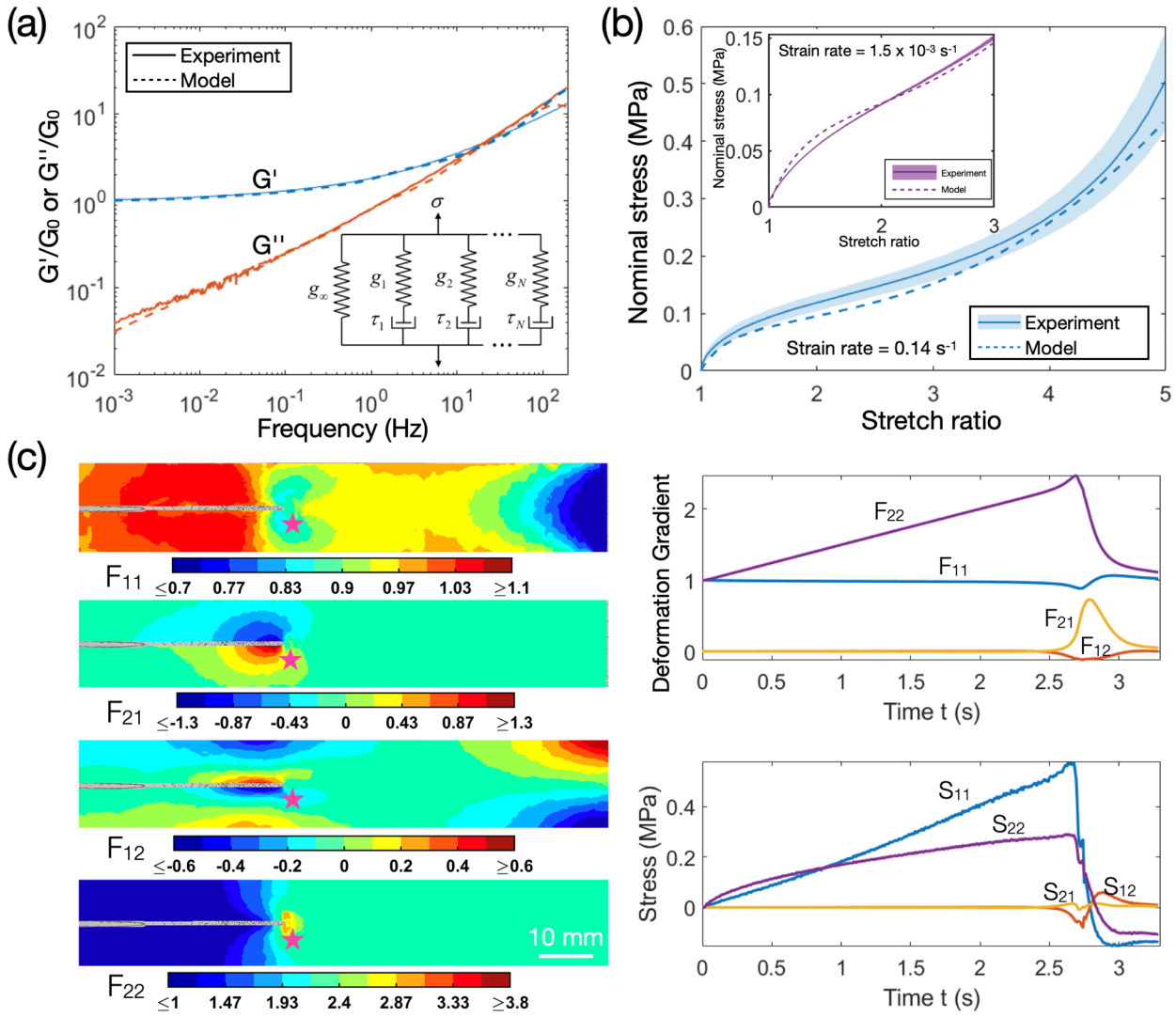

Figure 2 Constitutive modeling for the PSA. (a) Calibration of the relaxation function using DMA data in terms of the normalized storage and loss modulus versus loading frequency. The inset shows a schematic of the visco-hyperelastic constitutive model, where the springs represent elastic components given by a polynomial hyperelastic model and dash pots represent viscous components that result in relaxation. (b) Calibration of the hyperelastic parameters by fitting the constitutive model to uniaxial tensile data with strain rate = 0.14 s^{-1} (main plot) and 1.5×10^{-3} s^{-1} (inset). The shade represents range of experimental data from five repeated tests and the solid curve represents mean values of these repeated tests. The dashed curve is given by the calibrated constitutive model. (c) Calculation of stresses from the measured deformation field and the constitutive model. Left: fields of in-plane deformation gradient components at t = 2.88 s in a representative experiment (loading rate = 0.5 s^{-1}). Right: the deformation history $\mathbf{F}(t)$ at a material point (marked as the star on the left panel) and the first Piola-Kirchhoff stress components calculated using $\mathbf{F}(t)$ and the calibrated constitutive model.

The constitutive model described above is set up for three-dimensional (3D) deformation gradient tensor **F**, while only the in-plane components of **F** (i.e., in the X_1-X_2 plane) are measured in our experiments. To adapt the constitutive model to 2D deformation, we assume plane stress and incompressibility for the thin PSA samples so that $F_{\alpha 3} = F_{3\alpha} = 0$ ($\alpha = 1, 2$) and $F_{33} = (F_{11}F_{22} - F_{12}F_{21})^{-1}$. Also, the plan stress condition implies the out-of-plane normal stress σ_{33} is zero, which allows us to determine the hydrostatic component σ^H as $\sigma^H = -\sigma_{33}^D$.

Once the relaxation function $g(t)$ and the elastic deviatoric stress $\boldsymbol{\sigma}_0^D(t)$ are specified, the Cauchy stress tensor $\boldsymbol{\sigma}(t)$ can be determined for any given deformation history **F**(t) using Eq. (6), Eq. (7) and $\sigma^H = -\sigma_{33}^D$. The first Piola-Kirchhoff stress tensor **S** can be calculated using

$$\mathbf{S} = \det(\mathbf{F})\boldsymbol{\sigma}\mathbf{F}^{-T} = \boldsymbol{\sigma}\mathbf{F}^{-T}, \tag{8}$$

where we have used the incompressibility condition to set det (**F**) = 1. In the following we specify the relaxation function $g(t)$ and the hyperelastic model to determine the elastic deviatoric stress.

For the relaxation function $g(t)$, we adopt the following form based on the Prony series:

$$g(t) = g_\infty + \sum_{i=1}^{N} g_i e^{-t/\tau_i}, \tag{9}$$

where τ_i are the relaxation times and the coefficients g_i satisfy $\sum_{i=1}^{N} g_i = 1 - g_\infty$ such that $g(t=0) = 1$.

For the hyperelastic model, we adopt the incompressible polynomial model with the following strain energy density function W(**F**):

$$W(\mathbf{F}) = \sum_{i+j=1}^{M} C_{ij}(I_1 - 3)^i (I_2 - 3)^j, \tag{10}$$

where I_1 and I_2 are the first and second invariants of the left Cauchy-Green tensor $\mathbf{B} \equiv \mathbf{F}\mathbf{F}^T$, respectively. We choose $M = 2$ and the strain energy density W becomes:

$$W = C_{10}(I_1 - 3) + C_{01}(I_2 - 3) + C_{11}(I_1 - 3)(I_2 - 3) + C_{20}(I_1 - 3)^2 + C_{02}(I_2 - 3)^2. \tag{11}$$

The corresponding Cauchy stress tensor is given by

$$\boldsymbol{\sigma}_0 = -p\boldsymbol{\delta} + 2\left(\frac{\partial W}{\partial I_1} + I_1\frac{\partial W}{\partial I_2}\right)\mathbf{B} - 2\frac{\partial W}{\partial I_2}\mathbf{B}\mathbf{B}, \tag{12}$$

where p is the Lagrange multiplier to enforce the incompressibility constraint. The deviatoric component of $\boldsymbol{\sigma}_0$ is $\boldsymbol{\sigma}_0^D$ in which the Lagrange multiplier p is canceled out:

$$\boldsymbol{\sigma}_0^D = dev\left(\boldsymbol{\sigma}_0\right) = dev\left[2\left(\frac{\partial W}{\partial I_1} + I_1\frac{\partial W}{\partial I_2}\right)\mathbf{B} - 2\frac{\partial W}{\partial I_2}\mathbf{B}\mathbf{B}\right]. \tag{13}$$

By plugging the history data of $\mathbf{F}(t)$ into Eq. (13), we obtain the full history of the elastic deviatoric stress $\boldsymbol{\sigma}_0^D(t)$ which is then used in Eq. (7) to determine the deviatoric stress $\boldsymbol{\sigma}^D(t)$.

Table 1 Calibrated parameters of the constitutive model

Parameters for the relaxation function									
g_∞	g_1	g_2	g_3	g_4	g_5	g_6	g_7	g_8	g_9
0.032	0.844	0.072	0.036	9.4×10^{-3}	4.8×10^{-3}	1.4×10^{-3}	9.8×10^{-10}	1.4×10^{-3}	2.7×10^{-13}
	τ_1 (s)	τ_2 (s)	τ_3 (s)	τ_4 (s)	τ_5 (s)	τ_6 (s)	τ_7 (s)	τ_8 (s)	τ_9 (s)
	10^{-3}	10^{-2}	10^{-1}	1	10	10^2	10^3	10^4	10^5

Parameters for the hyperelastic model				
C_{10} (MPa)	C_{01} (MPa)	C_{20} (MPa)	C_{11} (MPa)	C_{02} (MPa)
-10^{-4}	1.148	0.023	-10^{-4}	-10^{-4}

Parameters of the constitutive model were calibrated by two sets of experimental data. First, the relaxation function $g(t)$ in Eq. (9) was calibrated using the DMA data under oscillatory shear (see Section 2.1). After the time-temperature shift, the DMA data covered a wide range of frequency (10^{-4} Hz to ~ 7.5×10^{12} Hz) at room temperature (25 ºC). However, fitting the entire frequency range of the DMA data would require many terms in the Prony series, i.e., $N = 17$ with τ_i ranging from 10^{-11} s to 10^5 s. Moreover, numerical evaluation of the convolution integral in Eq. (7) needs to be carried out with a time increment less than the shortest relaxation time (10^{-11} s), which could lead to extremely high computational cost especially for experiments with low loading rates. Therefore, instead of using the entire frequency range of the DMA data, we chose a subset

of the DMA data between 10^{-3} Hz and 200 Hz to calibrate $g(t)$. This frequency interval was selected according to the time derivative of deformation gradient $\mathbf{F}$, i.e., the deformation gradient rate $\dot{\mathbf{F}}$ ($=d\mathbf{F}/dt$), measured in our experiments. For example, $\dot{F}_{22}$, which is the dominant component of $\dot{\mathbf{F}}$, was found to range from ~ 0.005 s^{-1} to ~ 100 s^{-1} from our particle tracking measurements. Note that $\dot{F}_{22}$ near the crack tip can be higher than the loading rate (0.005 s^{-1} to 1 s^{-1}) because of the strain concentration and the fast crack propagation speed. Figure 2a shows the storage and the loss shear modulus *G'* and *G"* within the frequency internal of 10^{-3} Hz and 200 Hz at room temperature (25 ºC). Given the dimensionless nature of the relaxation function $g(t)$, we have normalized *G'* and *G"* by the storage modulus at the lower end of the frequency interval (i.e., 10^{-3} Hz), which is denoted as G_0 (= 58.6 kPa). The normalized data of *G'* and *G"* can be well fitted by Eq. (9) with $N = 9$ and parameters shown in Table 1. Second, the second-order polynomial hyperelastic model in Eq. (11) was calibrated using uniaxial tension data under three different strain rates spanning two orders of magnitude, i.e., 1.5×10^{-3} s^{-1}, 0.015 s^{-1}, 0.14 s^{-1} (see Section 2.1). The calibrated parameters for the hyperelastic model are also listed in Table 1. Using these parameters, the constitutive model can capture the uniaxial tensile data under all three strain rates. For example, comparisons between the model and the uniaxial tensile data under the highest strain rate (0.14 s^{-1}) and the lowest strain rate (1.5×10^{-3} s^{-1}) are shown in the main plot and the inset of Fig.2b, respectively.

It should be emphasized that the consitituive model adopted in this work (Simo, 1987) is an extension of linear viscoelasticity to accommodate large deformation. It does not include any coupling between the relaxation function and the level of deformation or stress, i.e., the relaxation function is independent of deformation. In general, the potential coupling between relaxation kinetics and deformation, if it exists, needs to be considered especially for material points near the crack tip (Knauss, 2015). However, this remains an open question due to difficulties in both experimental characterization and theoretical modeling of nonlinear viscoelasticity (Knauss, 2015). Nevertheless, the calibrated constitutive model is capable of capturing the PSA's viscoelastic behavior relevant to the fracture tests. While the DMA data used to calibrate the relaxation function were limited to small strain (< 5% as stated in Section 2.1), the uniaxial tensile data covered the regime of large strain (see Fig.2b). The maximum stretch ratio in the uniaxial tensile data ranges from 3 to 5, which is comparable to the level of deformation in our fracture tests. To illustrate the deformation fields in the fracture tests, we use a representative experiment with the loading rate

being 0.5 s^{-1}, and plot the fields of in-plane components of **F** at a particular time frame in the reference configuration (see Fig.2c). In particular, the value of F_{22} near the crack tip is ~ 3.

Equipped with the calibrated constitutive model, we can calculate the stress fields using the measured deformation gradients **F**(t). To demonstrate the calculation of stress components, we consider a specific material point (marked by a star in the deformation fields of Fig.2c) and plot the full history of all the in-plane deformation gradient components. The first Piola-Kirchhoff stress components are obtained by substituting the deformation history **F**(t) into the constitutive model in Eq. (7) and are shown in Fig.2c. Through this process we are able to obtain the full stress history at any given material point. As mentioned earlier, the time increment for numerically computing the convolutional integral in Eq. (7) is limited by the shortest relaxation time $\tau_1 = 10^{-3}$ s. As a result, the stress calculation was more computationally expensive for experiments with lower loading rates because of the longer time span. However, the shortest relaxation time τ_1 corresponds to the high frequency response, and thus is not as relevant in experiments with low loading rates. We found that the computational cost of stress calculation can be drastically reduced without affecting the result by recalibrating the constitutive model with the shortest relaxation time capped at 10^{-2} s (Appendix A). This reduced constitutive model was applied to experiments with loading rates below 0.5 s^{-1}.

3. Evolution of Displacement, Deformation and Stress Fields

Figure 3 illustrates how the displacement, deformation and stress fields evolve during crack propagation using five time frames from a representative fracture experiment (loading rate $\dot{\Delta}/H_0 = 0.5\ s^{-1}$). We choose the displacement component u_2 (Fig.3a), the deformation gradient component F_{22} (Fig.3b), and the first Piola-Kirchhoff stress component S_{22} (Fig.3c) to represent the displacement, deformation and stress fields, since they are the dominating components for Mode-I cracks. All fields are plotted in the reference configuration to facilitate comparison. A movie showing the continuous evolution of these fields in the deformed configuration is included in the Supplementary Materials (Supplementary Movie S1).

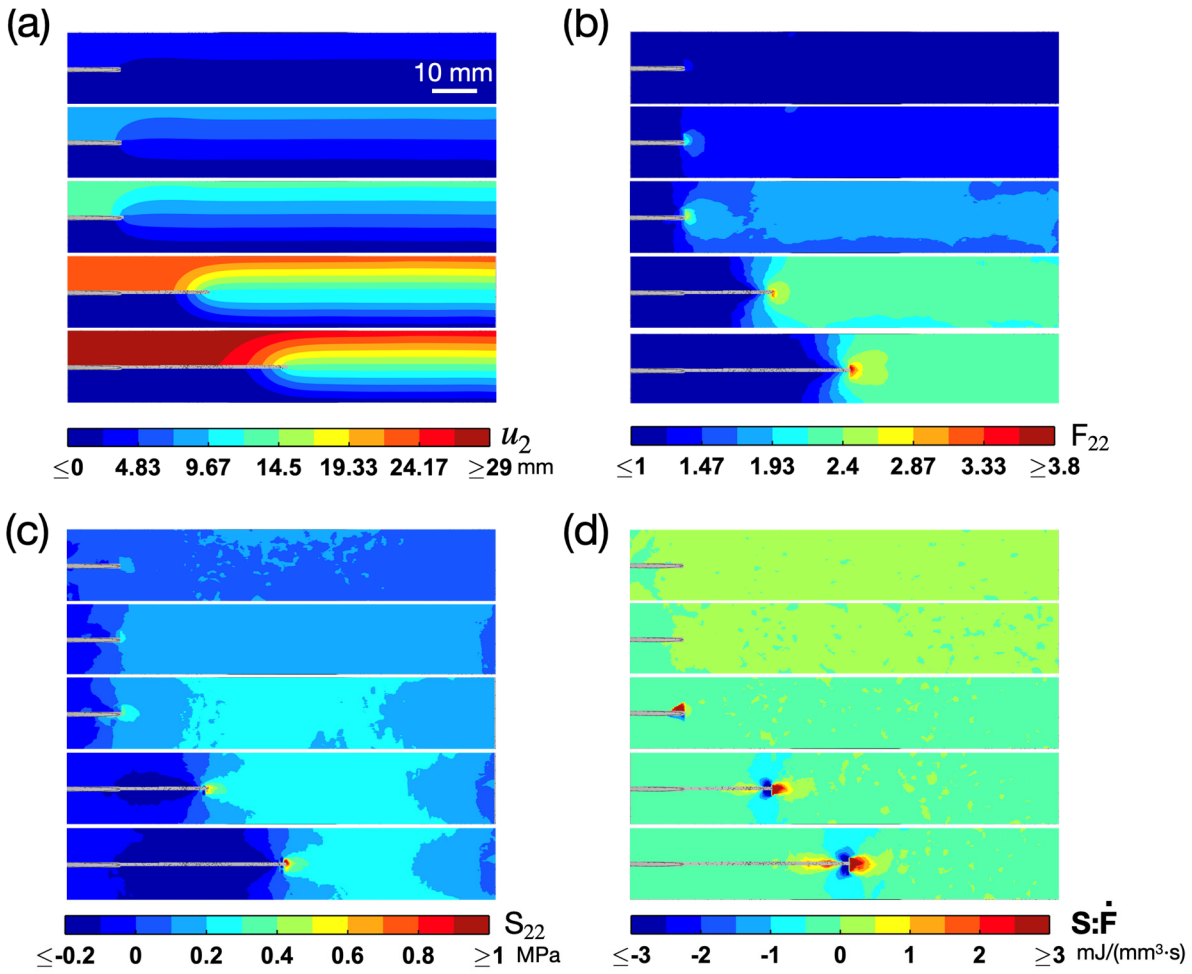

Figure 3 Evolution of fields in a representative experiment (loading rate = 0.5 s^{-1}) shown in terms of (a) the displacement u_2, (b) the deformation gradient F_{22}, (c) the stress S_{22}, and (d) the internal stress power density. All contour plots are shown in the reference configuration and the corresponding time frames from the top to bottom is t = 0.41s, 0.99s, 1.49s, 2.58s and 2.91s.

The displacement field (Fig.3a) exhibits a discontinuity across the crack, which is due to the opening of the crack under the applied tensile loading. Ahead of the crack tip, a positive gradient of u_2 along the X_2-direction is observed, consistent with the expectation that the material ahead of the crack tip is primarily subjected to a stretch along the X_2-direction. This is confirmed by the F_{22} fields in Fig.3b showing an approximately uniform distribution ahead of the crack tip. The value of F_{22} ahead of the crack tip increases with time because of the monotonic tensile loading. Around the crack tip, F_{22} is highly concentrated. In addition, the concentration of F_{22} near the crack tip continues to intensify in first three time frames during which the length of crack propagation was

small. In the last two time frames, the crack propagated significantly and the concentrated pattern of F_{22} is found to translate with the crack tip.

The fields of stress component S_{22} shown in Fig.3c are calculated using the calibrated constitutive model and the measured deformation gradient $\mathbf{F}(t)$. Similar to the F_{22} fields, the stress S_{22} is also concentrated at the crack tip. More importantly, the stress fields, when combined with the deformation fields, enables quantitative examination of the energy transfer associated with crack propagation. Specifically, the double inner product $\mathbf{S}:\dot{\mathbf{F}}$ is the internal stress power density at a material point. Recall that $\dot{\mathbf{F}} = d\mathbf{F}/dt$ is the time derivative of the deformation gradient $\mathbf{F}$. Physically $\mathbf{S}:\dot{\mathbf{F}}$ is the work density (i.e., per unit reference volume) done to a material point by its surrounding in a unit time. Positive $\mathbf{S}:\dot{\mathbf{F}}$ implies that the material point's surrounding is doing positive work to it (i.e., loading), while negative $\mathbf{S}:\dot{\mathbf{F}}$ implies the material point is doing positive work to its surrounding (i.e., unloading). Figure 3d shows evolution of the $\mathbf{S}:\dot{\mathbf{F}}$ field in the reference configuration. The continuous evolution of the $\mathbf{S}:\dot{\mathbf{F}}$ field in the deformed configuration is shown in the Supplementary Movie S1. No obvious pattern is observed in the first two time frames when the crack propagation was insignificant. In contrast, in the last two time frames the $\mathbf{S}:\dot{\mathbf{F}}$ field features a distinct pattern near the crack tip. In front of the crack tip there is a region of positive $\mathbf{S}:\dot{\mathbf{F}}$ indicating the material points there were experiencing loading. Behind the crack tip there are two symmetric regions of negative $\mathbf{S}:\dot{\mathbf{F}}$ indicating unloading behind the crack tip. As shown in the next section, the areal integral of the $\mathbf{S}:\dot{\mathbf{F}}$ field provides the net energy transfer within the PSA sample during crack propagation, which is necessary for determining the energy consumed at the crack tip (i.e., the intrinsic toughness).

4. Energetic Analysis and Fracture Toughness

4.1 Energy balance during crack propagation

To determine the intrinsic toughness Γ_0, we follow the energy balance theory in Qi et al. (2018), which leads to the following equation during quasi-static crack propagation:

$$\int_{\Omega} \mathbf{T}\cdot\frac{d\mathbf{u}}{dt}d\Omega - \int_{\Pi} \mathbf{S}:\frac{d\mathbf{F}}{dt}d\Pi = \Gamma_0\frac{d\Xi}{dt}, \tag{14}$$

where Π is the volume of a solid body in the reference configuration, Ω is the corresponding boundary surface, $\mathbf{T}$ is the traction vector, $\mathbf{u}$ is the displacement vector, Γ_0 is the intrinsic fracture toughness, Ξ is the crack surface area measured in the reference configuration. Eq. (14) is essentially a statement of mechanical energy balance in the solid (Holzapfel, 2002). The first integral on the left hand side of Eq. (14) is the power of external work to the solid, and the second integral is the power of net internal stress work within the solid. Their difference is the power consumed at the crack tip during crack propagation. If there is no crack propagation, $d\Xi/dt$ vanishes and thus Eq. (14) recovers the mechanical energy balance equation for solids under quasi-static deformation and without body forces (Holzapfel, 2002).

Using the plane stress condition for the thin PSA sheets in our experiments, we can simplify Eq. (14) into the following form by cancelling the sample thickness from both sides of the equation:

$$\int_{\partial A} \mathbf{T} \cdot \frac{d\mathbf{u}}{dt} dl - \iint_{A} \mathbf{S} : \frac{d\mathbf{F}}{dt} dA = \Gamma_0 \frac{dC}{dt}, \tag{15}$$

where A is the surface area of the PSA sample, ∂A represents the boundary of A (Fig.4a), and C is the length of crack propagation measured in the reference configuration (Fig.4a). Evaluation of the time derivatives in Eq. (15) from two consecutive time frames is sensitive to uncertainties in the particle tracking data and numerical errors in the stress calculation. To circumvent this difficulty, we introduce the cumulative external work W_{ext} and the cumulative stress work W_{int} as

$$W_{\text{ext}} = \int_0^t \left(\int_{\partial A} \mathbf{T} \cdot \frac{d\mathbf{u}}{dt} dl \right) dt, \tag{16}$$

$$W_{\text{int}} = \int_0^t \left(\iint_{A} \mathbf{S} : \frac{d\mathbf{F}}{dt} dA \right) dt. \tag{17}$$

Combining Eqs. (15), (16) and (17), we obtain the following equation for the intrinsic toughness:

$$\Gamma_0 = \frac{d\left(W_{\text{ext}} - W_{\text{int}}\right)}{dC}. \tag{18}$$

Eq. (18) suggests that Γ_0 is equal to the slope of the $W_{\text{ext}} - W_{\text{int}}$ versus C curve. This approach enables us to average over different time frames and hence reduce the impact of measurement uncertainties and numerical errors. As shown in Fig.3d, the field of $\mathbf{S}:\dot{\mathbf{F}}$ is obtained at all time

frames. By integrating $\mathbf{S}$: $\dot{\mathbf{F}}$ over the sample surface and over time, we obtain W_{int} at all time frames. For W_{ext}, we first calculate the traction vector $\mathbf{T}$ on the boundary as $\mathbf{T} = \mathbf{S} \cdot \mathbf{n}$ where $\mathbf{n}$ is the unit outward normal vector on the boundary in the reference configuration, then obtain the velocity vector $d\mathbf{u}/dt$ on the boundary (e.g., see the velocity field in Fig.1d), and finally integrate $\mathbf{T} \cdot (d\mathbf{u}/dt)$ over the boundary and over time to obtain W_{ext}.

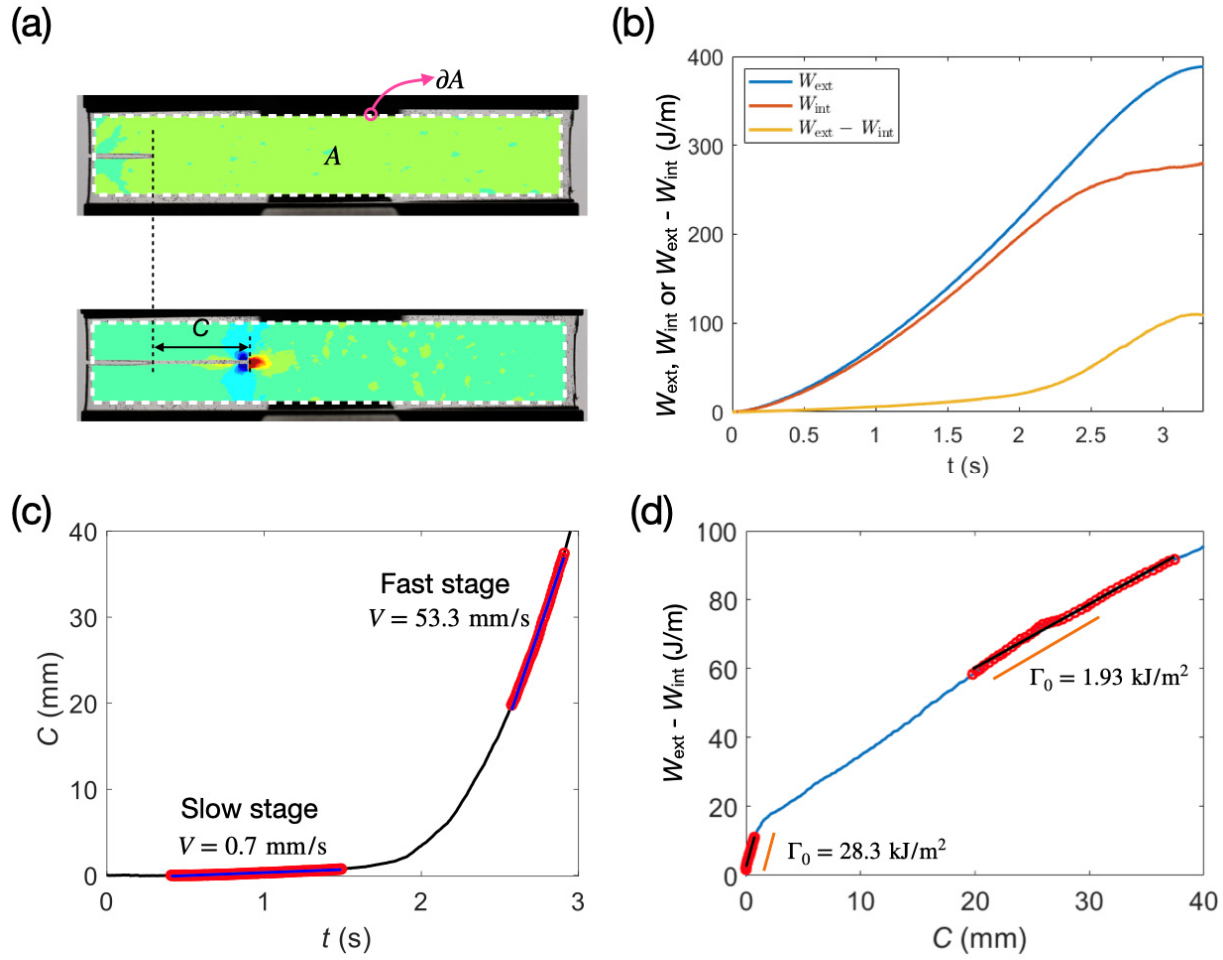

Figure 4 Determination of the intrinsic toughness Γ_0 using a representative experiment (loading rate = 0.5 s^{-1}). (a) The length of crack propagation C is measured in the reference configuration. The two contour plots illustrate the distributions of $\mathbf{S}$: $\dot{\mathbf{F}}$ in reference configuration at (top) t = 0.41 s and (bottom) t = 2.58 s. The contour plots also illustrate the integration region for obtaining W_{int} and its boundary (dashed lines) for obtaining W_{ext}. (b) History of W_{ext}, W_{int} and $W_{\text{ext}} - W_{\text{int}}$. (c) History of the crack propagation length C showing two stages of crack propagation (i.e., slow and fast). (d) The slope of the $W_{\text{ext}} - W_{\text{int}}$ versus C curve is extracted as the intrinsic toughness Γ_0.

Example results for W_{ext}, W_{int} and $W_{\text{ext}} - W_{\text{int}}$ in a representative experiment (loading rate $\dot{\Delta}/H_0$ = 0.5 s^{-1}) are shown in Fig.4b. Initially ($t < \sim 0.5$ s), W_{ext} and W_{int} are approximately equal, indicating that the crack has not propagated yet. After t = 0.5 s, W_{ext} becomes larger than W_{int}, thus resulting in an excessive amount of energy ($W_{\text{ext}} - W_{\text{int}} > 0$) consumed by crack propagation. To determine the intrinsic toughness, we obtain the length of crack propagation C over time (Fig.4c) and plot $W_{\text{ext}} - W_{\text{int}}$ against C in Fig.4d. Interestingly, Fig.4c shows that there are two stages of crack propagation. Before $t = \sim 2$ s, the crack underwent a stage of slow propagation with a speed of $V \equiv dC/dt$ = 0.7 mm/s. After $t = \sim 2$ s the crack propagation transitioned to a fast stage with a speed of V = 53.3 mm/s. The two stages of crack propagation are also manifested in the $W_{\text{ext}} - W_{\text{int}}$ versus C curve (Fig.4d), which consists of two segments (approximately linear) with distinct slopes. The segment corresponding to the slow stage has a higher slope than the segment corresponding to the fast stage. By performing linear fits to the two segments and obtaining their slopes, we found two values of intrinsic toughness: Γ_0 = 28.3 kJ/m^2 for the slow stage and Γ_0 = 1.9 kJ/m^2 for the fast stage. The stark contrast in Γ_0 between the two stages of crack propagation indicates it may not be a material constant, which will be further discussed in Section 4.2.

Our method for extracting Γ_0 relies on two key inputs: 1) experimentally measured fields of displacement **u** and deformation gradient **F**, and 2) a constitutive model to enable the computation of stress **S**, traction **T** and internal stress power density $\mathbf{S}:\dot{\mathbf{F}}$. Since the deformation field is measured from experiments, no assumption is needed for the crack propagation (e.g., the steady-state assumption). Therefore, this method can be extended to any fracture test geometry and loading history as long as full-field and full-history measurements of **u** and **F** are available. In addition, the constitutive model is only used to calculate the stress **S** and does not need to provide any interpretation for the stored energy and dissipation. This feature allows one to apply phenomenological models such as the one described in Section 2.5.

4.2 Two stages of crack propagation

We conducted a series of fracture experiments with the loading rate $\dot{\Delta}/H_0$ ranging from 0.005 s^{-1} to 1 s^{-1}. Among all these experiments, the two stages of crack propagation were consistently observed. The crack propagation speeds in both stages increased as the loading rate was increased.

Following the same data processing method described in Section 4.1, we extracted the intrinsic toughness Γ_0 and the crack propagation speed V for both stages in each experiment and plotted the results in Fig.5.

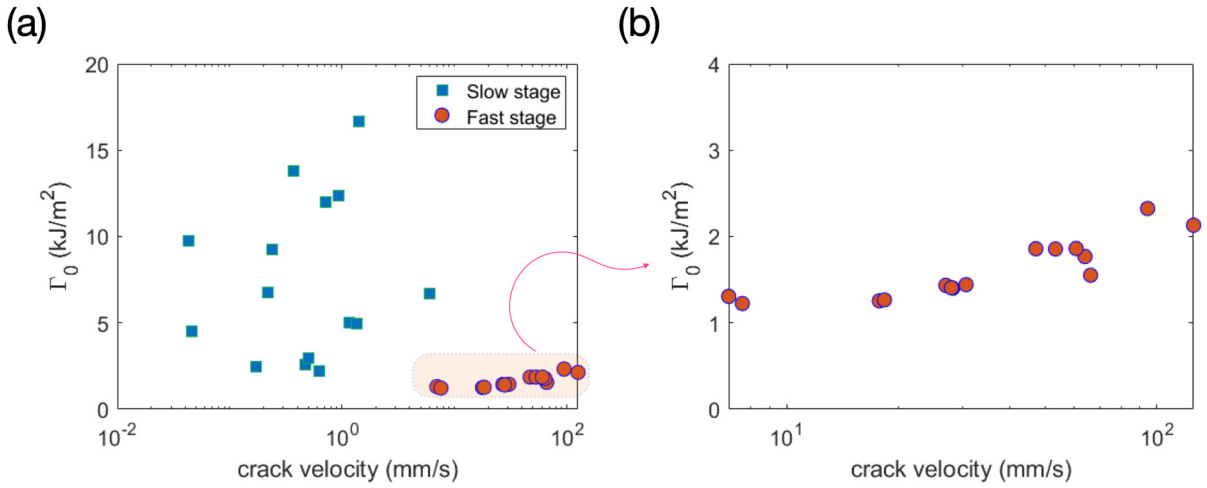

Figure 5 Intrinsic toughness of the two stages of crack propagation. (a) Intrinsic toughness Γ_0 versus crack propagation speed V for both the slow propagation (blue squares) and fast propagation stages (red circles). (b) Zoomed-in view of the Γ_0 versus V data for the fast propagation stage.

As shown in Fig.5a, the crack propagation speed for the slow stage falls into the range of 0.04 ~ 6 mm/s. The intrinsic toughness Γ_0 exhibits a large range of variation from 2 to 20 kJ/m^2, and does not show any correlation with the crack propagation speed V. In contrast, the Γ_0 versus V data for the fast stage (Fig.5b) feature a clear trend. Specifically, as the crack propagation speed V increased from ~7 to ~120 mm/s, Γ_0 increased from ~1.3 to ~2 kJ/m^2. This range is much smaller than that found for the slow stage. Since the deformation field **F** was obtained by interpolating the tracer particle displacements, its spatial resolution is limited by the spacing of tracer particles. Therefore, our method may not be able to resolve the highly concentrated deformation field in the vicinity of the crack tip. Recall that a strip-like gap with a height of 0.7 mm across the crack surfaces is excluded from the deformation field (see Section 2.4 and Fig.1d). Any viscoelastic dissipation occurring within this gap region is not included in our calculation, and hence is lumped into Γ_0. This could explain the slight dependence of Γ_0 on the crack propagation speed V for the fast stage. In summary, we draw two conclusions from Fig.5. First, the slow stage of crack

propagation in our experiments cannot be represented by a constant intrinsic toughness. Second, the fast stage of crack propagation features an approximately constant intrinsic toughness Γ_0 (1.3-2 kJ/m^2) for crack speed between 7 and 120 mm/s.

It is worth mentioning that the intrinsic toughness Γ_0 for the fast stage of crack propagation is much larger than the intrinsic toughness Γ_{LT} given by the Lake-Thomas model, which is typically on the order of 10 ~ 100 J/m^2 (Creton and Ciccotti, 2016). To understand this discrepancy, we emphasize that Γ_0 in this work is defined relative to the bulk dissipation Γ_D and accounts for the crack tip fracture processes below the continuum scale, whereas Γ_{LT} by the Lake-Thomas model is due to the chain scission occurring over one mesh size of the polymer network. The large gap between the two length scales underlying Γ_0 and Γ_{LT} leaves room for additional fracture processes. As discussed in Section 1, it has been experimentally observed that chain scission can occur in a delocalized manner over hundreds of micrometers away from the crack (Slootman et al., 2020). Such delocalized damage could be caused by network imperfection (Yang et al., 2019). A recent work by Lin et al. (2022) showed that delocalized damage contributes to a "near-tip dissipation" term Γ_D^{tip} in addition to the Lake-Thomas term Γ_{LT}. The Γ_0 defined in our work should be interpreted as $\Gamma_{LT} + \Gamma_D^{tip}$ rather than Γ_{LT}. More recently, Deng et al. (2023) found that nonlocal energy release during the fracture of polymer-like networks is not captured by the Lake-Thomas model, causing Γ_{LT} to be significantly lower than Γ_0. Given that the molecular structure of commercial PSAs is not readily available, it can be difficult to directly estimate Γ_{LT}. To this end, it is worth mentioning that Lin et al. (2022) determined Γ_{LT} as the cyclic fatigue threshold (Bai et al., 2019b). Therefore, future work can be directed towards measuring the cyclic fatigue threshold for the PSAs and comparing it with the Γ_0 for continuous crack propagation, which is reminiscent of the contrast between the cyclic and the static fatigue thresholds (Bai et al., 2019a).

The two-stage crack propagation observed in our experiments should be distinguished from the delayed fracture reported for hydrogels (Tang et al., 2017; Bai et al., 2019b; Qi et al., 2024). Although both phenomena feature a transition from slow to fast crack propagation, delayed fracture occurs under a fixed global loading (Tang et al., 2017), whereas our experiments were conducted under a monotonically increasing global loading. The phenomenon of two-stage crack propagation similar to that found in our experiments has been reported for unfilled synthetic rubber

(Roucou et al., 2019). In their fracture experiments with pure-shear samples and monotonic loading, the crack first propagated slowly and then in a "quasi-instantaneous" manner. Interestingly, Roucou et al. (2019) found that the two stages of crack propagation can be differentiated based on the crack surface morphology: the slow propagation stage resulted in rough crack surfaces and the fast propagation stage caused smooth, mirror-like crack surfaces. This finding suggests that the two stages of crack propagation may be associated with different fracture processes at the crack tip. Motivated by this hypothesis, we performed additional experiments to gain insights towards the underlying mechanism of the two-stage crack propagation and the stark contrast in Γ_0 values, as detailed in the next section.

5. Mechanism for the Two-stage Crack Propagation

5.1 Onset of fast crack propagation

Examination of the post-mortem fracture surface, as shown in Fig.6a, reveals regions with distinct morphology. Surface of the initial crack is rough, presumably because it was introduced by cutting the PSA sample with a scissor. The fracture surface caused by the slow crack propagation is also rough, but the fracture surface caused by the fast crack propagation is much smoother (Fig.6a). Such transition from rough to smooth fracture surface closely resembles that described by Roucou et al. (2019), and supports the hypothesis that the two stages of crack propagation in our experiments are governed by different crack tip fracture processes.

The next question is what controls the transition from rough to smooth fracture surfaces. To answer this question, we plot the critical global stretch ratio $\lambda \equiv 1 + \Delta / H_0$ at the onset of fast crack propagation as a function of the loading rate $\dot{\Delta}/H_0$ in Fig.6b. For all experiments, the critical global stretch ratio is consistently found at ~ 2. Furthermore, we extract the value of F_{22} closest to the crack tip when the onset of fast crack propagation occurred, which can serve as an indication of the local stretch ratio at the crack tip. The data of the critical crack tip F_{22} are more scattered (Fig.6b), which is expected because of the uncertainties associated the particle tracking and interpolation processes. Despite the scattering, the critical crack tip F_{22} falls into 3 ~ 4.8 for a wide range of loading rates ($\dot{\Delta}/H_0$ = 0.005 to 1 s^{-1}), thereby suggesting that the transition from rough to smooth fracture is governed by a critical stretch at the crack tip. Since the pure-shear PSA samples

in our experiments were subjected to monotonic loading, the stretch at the crack tip should also increase accordingly. Once the critical stretch is reached, smooth fracture would occur.

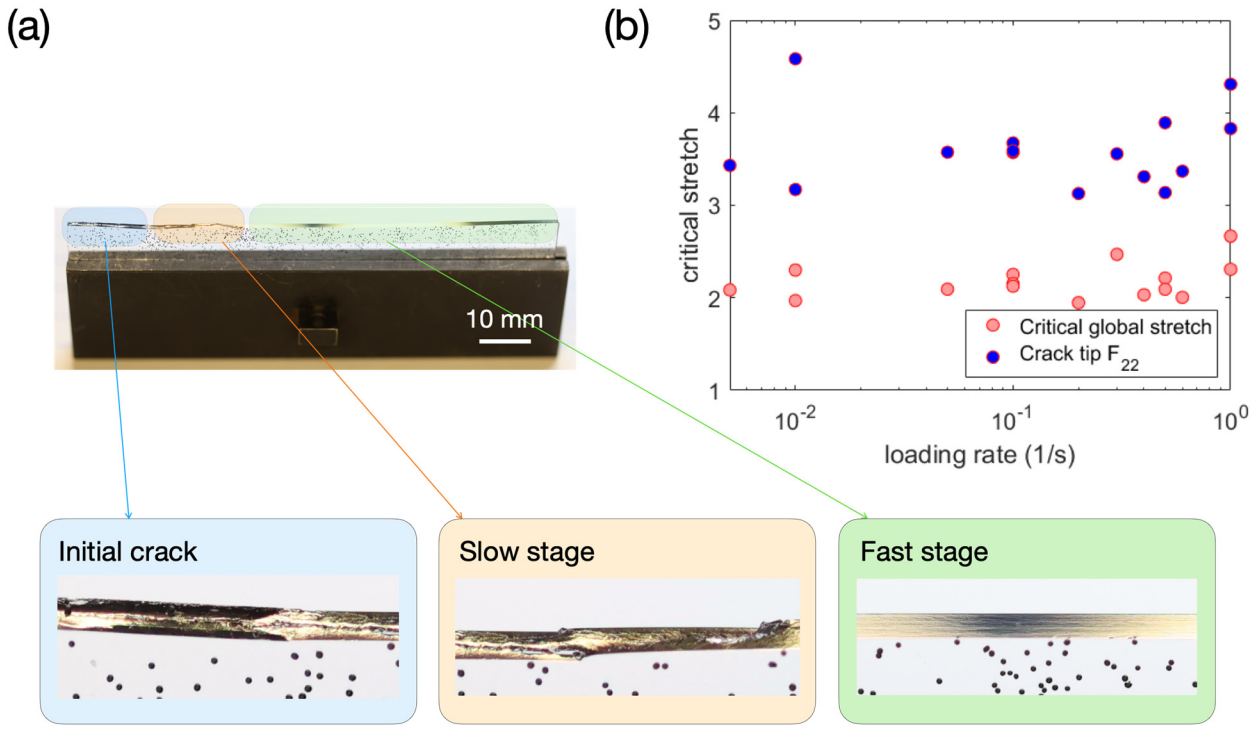

Figure 6 Two stages of crack propagation. (a) Post-mortem fracture surface of a representative experiment (loading rate = 0.005 s^{-1}) showing rough fracture surface for the slow propagation stage and smooth fracture surface for the fast propagation stage. (b) The critical global stretch ratio and the crack tip F_{22} at the onset of the fast propagation stage as a function of the loading rate.

5.2 Hypothesized mechanism

Based on the discussions in Section 5.1, we hypothesize the following mechanism for the two-stage crack propagation. Assume there exists a critical stretch governing material failure at the crack tip. The material at the crack tip breaks if this critical stretch is exceeded. However, in practice the initial crack introduced by a pair of scissors is not perfectly sharp and may not be uniform throughout the sample thickness. Therefore, we envision a three-dimensional (3D) tortuous surface profile instead of a sharp and straight front at the initial crack tip. The imperfect geometrical profile of the initial crack tip can lead to through-thickness variations in the tensile

deformation around the initial crack tip. Such variations amplify the stretch locally and thus may trigger material failure even when the average crack tip stretch is below the critical value.

Once localized failure is initiated at some point along the surface of the initial crack tip, the excessive load would be transferred to the rest of the initial crack tip surface, thereby causing a cascade of failure events and eventually inducing the slow crack propagation stage. This physical picture is similar to the subcritical fracture observed and characterized recently for soft elastomers (Ju et al., 2023). Furthermore, recall that the PSA samples in our experiments (~ 1-mm thick) were prepared by laminating 4 layers of PSA films. This lamination structure may also affect the load transfer process. Nevertheless, the slow propagation stage should involve a crack tip failure process that is non-uniform across the thickness and is sensitive to the geometric imperfection of the initial crack tip. This can explain the rough fracture surface and the highly scattered values of Γ_0 for the slow propagation stage.

As the global loading continues to increase, the critical stretch for material failure is exceeded and the fast propagation stage starts. In this stage, the crack tip failure process occurs simultaneously across the sample thickness, thus resulting in smooth fracture surfaces and consistent values of Γ_0 (Fig.5b). This also implies that the crack tip in the fast propagation stage is sharp. Consequently, the fast propagation stage involves a smaller length scale for the crack tip failure process and hence smaller Γ_0 values than the slow propagation stage.

5.3 Controlling the onset of fast crack propagation

We performed additional experiments to test the hypothesized mechanism for the two-stage crack propagation, as illustrated in Fig.7. Specifically, we applied the same experimental configuration as described in Section 2.2, but replaced the monotonic loading by a two-step loading history, i.e., a continuous loading step with constant loading rate (0.01 s^{-1}) followed by a holding step at a fixed global stretch ratio $\lambda = \lambda_{hold}$. By varying λ_{hold}, we can test if the onset of fast crack propagation can be controlled by altering the global stretch.

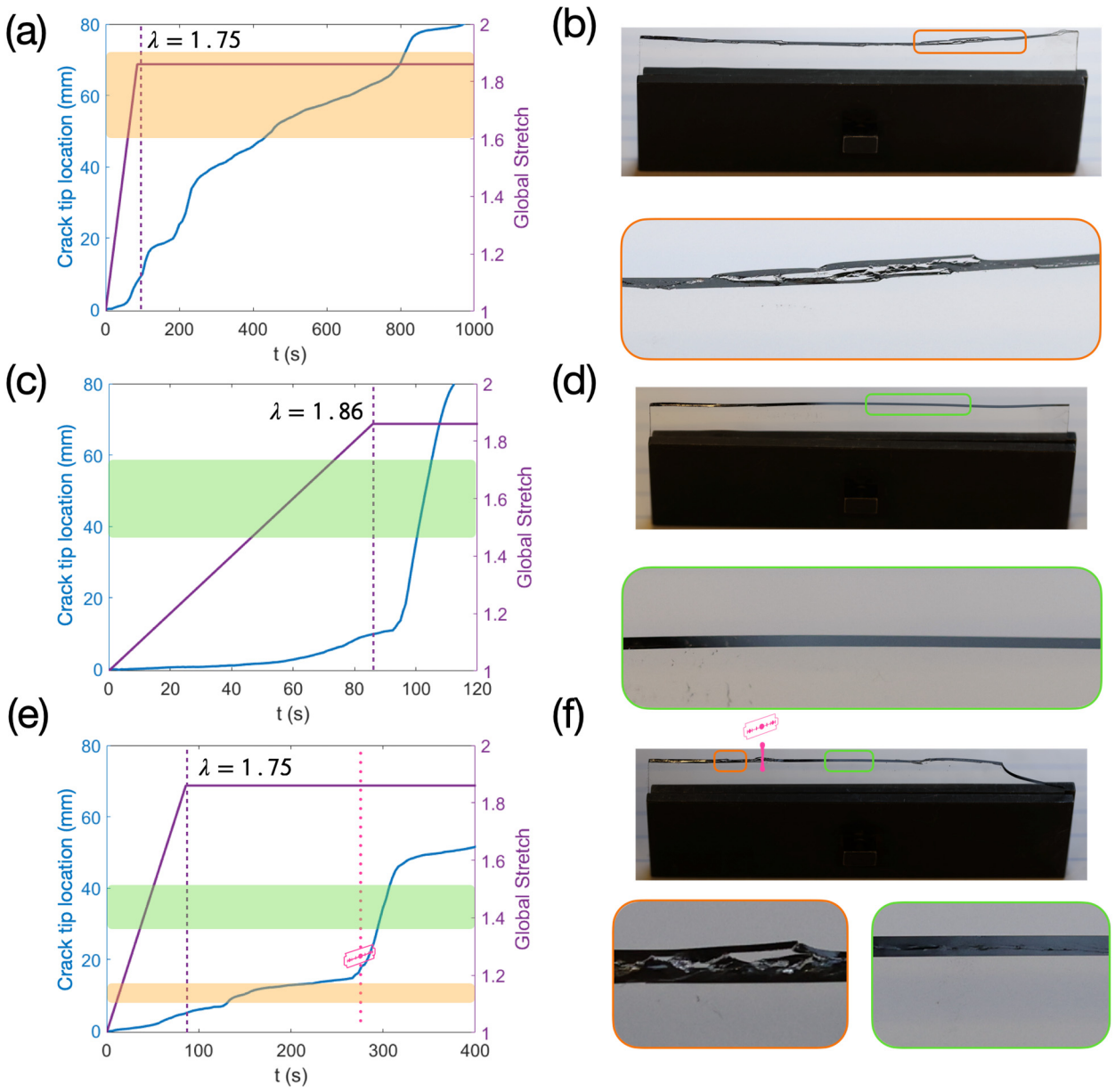

Figure 7 Controlling the onset of fast propagation using two-step loading tests with the initial loading rate of 0.01 s^{-1} and different λ_{hold}. (a)-(b) Result for λ_{hold} = 1.75: (a) loading history and crack tip location in the deformed configuration versus time, and (b) crack surface with a zoomed-in view for the segment (bounded by the orange rectangle) corresponding to the region in (a) highlighted in orange. (c)-(d) Result for λ_{hold} = 1.86: (c) loading history and crack tip location in the deformed configuration versus time, and (d) crack surface with a zoomed-in view for the segment (bounded by the green rectangle) corresponding to the region in (c) highlighted in green. (e)-(f) Result for λ_{hold} = 1.75 with an *in situ* cut to the blunted crack tip at t = ~ 200s: (e) loading history and crack tip location in the deformed configuration versus time, and (f) crack surface with a zoomed-in view for the segments (bounded by the orange and green rectangles) corresponding to the regions in (e) highlighted in orange and green. The razor blade symbol illustrates the point at which the *in situ* cut was introduced.

According to our hypothesis, the fast propagation stage should not occur if λ_{hold} is not sufficiently large. We set $\lambda_{hold} = 1.75$ which is below the critical global stretch at the onset of fast propagation (i.e., ~ 2 in Fig.6b). The loading history and the consequent crack propagation behavior are shown in Fig.7a. Since no tracer particles were used here, we were unable to determine the length of crack propagation C (Fig. 4a). Instead we use the horizontal coordinate of the crack tip in the deformed configuration to represent the extent of crack propagation (i.e., the "crack tip location" in Fig.7a). As expected from our hypothesis, no transition to the fast propagation stage was observed in this experiment. The entire course of crack propagation remained in the slow propagation stage. Although there were variations in crack speed (see the slope of the crack tip location versus time curve in Fig.7a), indicating that the crack propagated in a jigged manner, the average crack speed was ~ 0.1 mm/s, which falls into the range for the slow propagation stage. The slow propagation stage is further evidenced by the rough fracture surface found after this experiment (Fig.7b).

When λ_{hold} is increased, the fast propagation stage should emerge. To test this prediction, we increased λ_{hold} to 1.86 (Fig.7c). Note that we intentionally kept λ_{hold} smaller than 2 to avoid triggering the fast propagation stage prematurely in the continuous loading step. After the holding step started, the crack first underwent slow propagation for a few seconds and then suddenly transitions into the fast propagation stage (average crack speed = ~ 4 mm/s). Smooth fracture surface was found after this experiment (Fig.7d).

To further test our hypothesis, we repeated the experiment with $\lambda_{hold} = 1.75$. After the holding step started, the crack entered the slow propagation stage (similar to Fig.7a). After holding for ~ 200 seconds, we applied a small cut to the blunted crack tip *in situ* using a razor blade. This cut can disrupt the crack tip process associated with the slow propagation stage. In addition, since the material near the blunted crack tip is highly stretched and much thinner than the initial thickness, the *in situ* cut can induce a sharper crack tip, thus triggering the fast propagation stage. This was indeed observed in our experiment. After the cut was applied, the crack suddenly entered the fast propagation stage (Fig.7e), which lasted ~ 40 s before getting back to the slow propagation stage. The fracture surface also exhibits a transition from rough to smooth after the cut was applied. While observations in this experiment are consistent with our hypothesis, more thorough experiments need to be carried out in the future to draw conclusions on the different crack tip processes underlying the slow and fast propagation stages.

6. Conclusion

In this work we experimentally characterized the intrinsic toughness Γ_0 for a soft pressure sensitive adhesive (PSA). We performed pure shear fracture experiments under monotonic loading. Tracer particles were randomly deposited on the surface of the PSA samples. By tracking the tracer particles over the entire course of each experiment and interpolating their displacements, we obtained full-field and full-history data of the 2D displacement and deformation gradient fields in each fracture experiment. The deformation gradient data were then substituted into a calibrated nonlinear constitutive model from which the fields of stress and internal stress power density were calculated at each time frame. Finally, we integrated the internal stress power density both spatially and temporally, and determined the intrinsic toughness Γ_0. This process was repeated for fracture experiments with different loading rates to uncover the dependence of Γ_0 on the crack propagation speed.

The experimentally extracted values of Γ_0 provide useful insights towards the two-stage crack propagation behavior observed in our experiments. We found that under monotonic loading the initial crack first underwent a slow propagation stage and then suddenly entered a fast propagation stage. The Γ_0 values for the slow propagation stage are highly scattered and do not exhibit any correlation with the crack speed, whereas the Γ_0 values for the fast propagation stage remain consistently in the range of 1.3-2 kJ/m^2 and exhibit a slight increase with the crack speed. This contrast is in line with the distinct morphology of fracture surface for the two stages of crack propagation, i.e., rough fracture surface for the slow propagation and smooth fracture surface for the fast propagation. Additional experiments revealed that the onset of fast crack propagation can be controlled by altering the applied stretch or introducing an *in situ* cut to the blunted crack tip during the slow propagation stage. These findings suggest that the slow and fast propagation stages involve different crack tip fracture processes.

Although our fracture experiments were performed using the pure shear geometry under monotonic loading, our method for determining Γ_0 does not rely on any assumptions on the sample geometry or loading history. In principle, our method can be extended to any soft thin-sheet samples with arbitrary geometries and loading histories, as long as the particle tracking method can be applied and an accurate constitutive model is available. Moreover, since we can follow the crack trajectory by mapping the crack tip location in the deformed configuration to the reference

configuration, this method does not require a straight crack trajectory and thus can be applied beyond Mode-I loading (Lu et al., 2021). Therefore, this method can serve as a general tool for characterizing the intrinsic fracture toughness of soft materials. Experimental results on the intrinsic toughness can provide important insights towards understanding the crack tip fracture process or be used as inputs for computational modeling of crack propagation in soft materials.

Acknowledgement

X.Y. and R.L. acknowledge funding support from the 3M Company. R.L. is also supported by the National Science Foundation (NSF-CMMI-1752449).

Supplementary Materials

Movie S1: Evolution of the displacement u_2 field (top left), the deformation gradient F_{22} field (top right), the stress S_{22} field (bottom left), and the internal stress power density $\mathbf{S}:\dot{\mathbf{F}}$ field in the deformation configuration from a representative experiment (loading rate = 0.5 s^{-1}).

Appendix A: Reduced Constitutive Model

The constitutive parameters listed in Table 1 can provide good agreement between the model and the DMA and uniaxial tensile data. However, since the smallest relaxation time is 10^{-3} s, the number of time increments needed to numerically compute the convolution integral in Eq. (7) can be very large, because the time increment size should be much lower than the smallest relaxation time. This means the stress calculation process can be extremely time consuming for experiments with low loading rates. For example, experiments with the lowest loading rate (0.005 s^{-1}) lasted for ~200 s, which would require 2 million time increments for an increment size of 10^{-4} s. To balance accuracy and efficiency for experiments with low loading rates, we recalibrated the constitutive model with the smallest relaxation time capped at 0.01 s. This would allow us to use larger time increments for evaluating Eq. (7) and hence reduce the computational cost of stress calculation. Also, increasing the shortest relaxation time from 10^{-3} s to 0.01 s does not affect the results of stress and energetics for experiments with low loading rates, because the relaxation time

of 10^{-3} s corresponds to the material's response at high strain rate (e.g., on the order of $10^2 \sim 10^3$ s^{-1}) which is well beyond the range for experiments with low loading rates.

In the following, we will refer to the constitutive model with the shortest relaxation time of 0.01 s as the reduced model. Parameters for the reduced model were calibrated following similar procedures in Section 2.5 and are listed in Table 2. Figure 8 shows the comparison between the reduced model and the DMA data or the original model (Table 1). First, as expected, the reduced model does not capture the DMA data at high frequency (~10 to 100 Hz) because the relaxation time is capped at 0.01 s (Fig.8a). However, it still provides a good agreement with the DMA data when the frequency is below 10 Hz (Fig.8a). Second, the reduced model gives almost identical stress-stretch curve under uniaxial tension as the original model under a strain rate of 0.14 s^{-1} (same as the main plot of Fig.2b) and a higher strain rate (1 s^{-1}) (Fig.8b). Third, we utilized both the reduced and original models to process a representative experiment with the loading rate being 0.5 s^{-1}. As shown in Fig.8c, the $W_{\text{ext}} - W_{\text{int}}$ versus C curves obtained from the two models agree well initially, and exhibit a slight discrepancy when the fast propagation stage ocurred. This is expected because the fast propagation stage entails higher strain rate near the crack tip. Nevertheless, the intrinsic toughness Γ_0 for the fast propagation stage is 1.93 kJ/m^2 based on the original model, and is 2.09 kJ/m^2 based on the reduced model, exhibiting a relative difference of ~8%. However, the computational time was reduced from ~2 weeks with the original model to ~36 hours with the reduced model. This drastic improvement in computational efficiency motivated us to adopt the reduced model for all experiments with loading rates below 0.5 s^{-1}.

Table 2 Calibrated parameters of the reduced constitutive model

Parameters for the relaxation function								
g_∞	g_1	g_2	g_3	g_4	g_5	g_6	g_7	g_8
0.104	0.769	0.0663	0.0358	0.0152	4.7×10^{-3}	4.51×10^{-9}	4.6×10^{-3}	5.26×10^{-12}
	τ_1 (s)	τ_2 (s)	τ_3 (s)	τ_4 (s)	τ_5 (s)	τ_6 (s)	τ_7 (s)	τ_8 (s)
	10^{-2}	10^{-1}	1	10	10^2	10^3	10^4	10^5

Parameters for the hyperelastic model				
C_{10} (MPa)	C_{01} (MPa)	C_{20} (MPa)	C_{11} (MPa)	C_{02} (MPa)
-10^{-4}	0.4313	0.0069	-10^{-4}	-10^{-4}

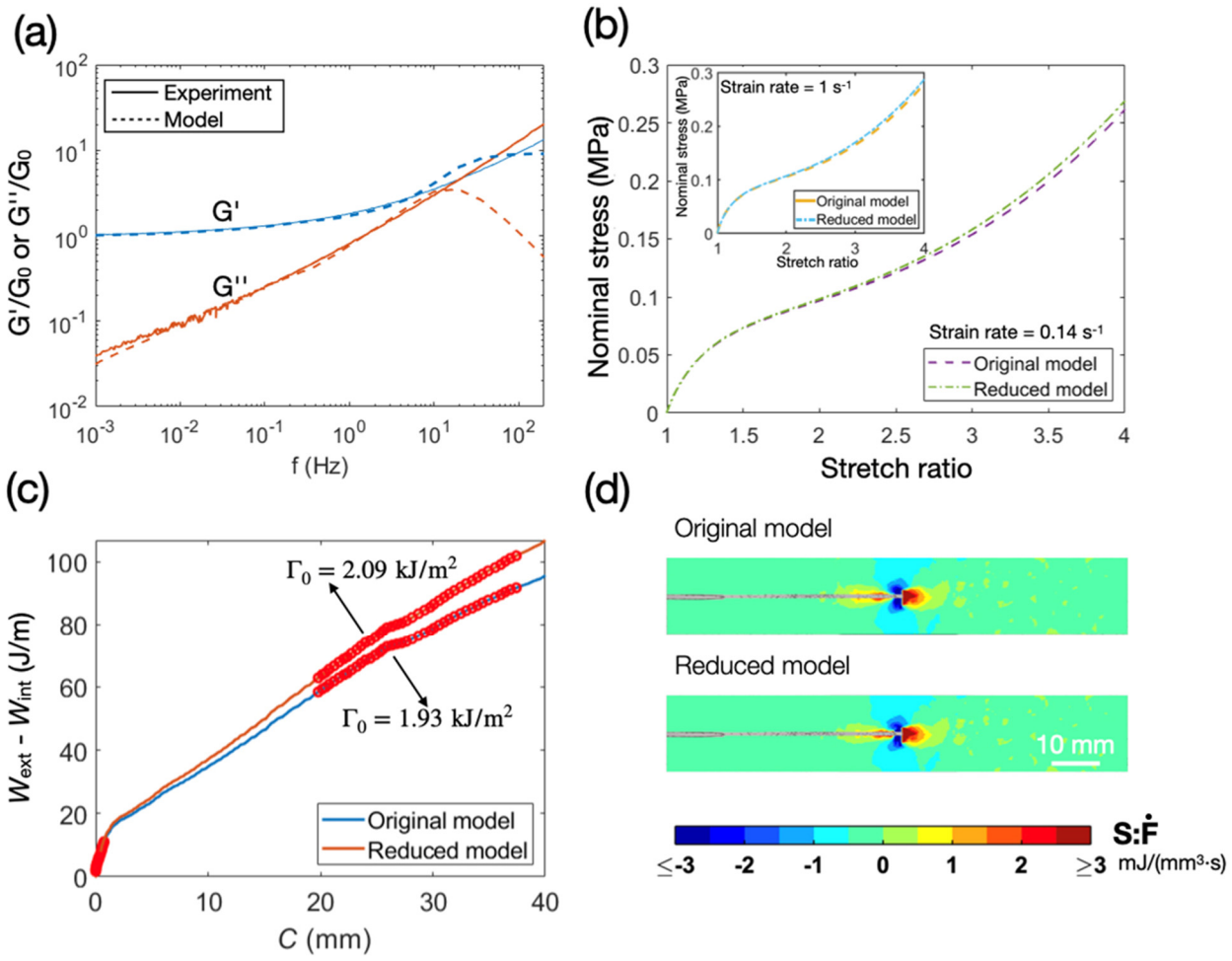

Figure 8 Reduced constitutive model. (a) Comparison between the relaxation function of the reduced model (Table 2) to the normalized DMA data. (b) Comparison between the reduced model (Table 2) and the original model (Table 1) under uniaxial tension with strain rate = 0.14 s^{-1} (main plot) and 1 s^{-1} (inset). (c) The $W_{ext} - W_{int}$ versus C curve and the intrinsic toughness in the fast propagation stage based on the reduced model and the original model for an experiment with a loading rate of 0.5 s^{-1}. (d) Contour of the internal stress power density obtained for an experiment with a loading rate of 0.5 s^{-1} at t = 2.91s using the reduced model and the original model.

References

Ahagon, A., Gent, A.N., 1975. Threshold fracture energies for elastomers. J. Polym. Sci. Polym. Phys. Ed. 13, 1903–1911. https://doi.org/10.1002/pol.1975.180131005

Akagi, Y., Sakurai, H., Gong, J.P., Chung, U. Il, Sakai, T., 2013. Fracture energy of polymer gels with controlled network structures. J. Chem. Phys. 139, 144905. https://doi.org/10.1063/1.4823834

Bai, R., Chen, B., Yang, J., Suo, Z., 2019a. Tearing a hydrogel of complex rheology. J. Mech. Phys. Solids 125, 749–761. https://doi.org/10.1016/J.JMPS.2019.01.017

Bai, R., Yang, J., Suo, Z., 2019b. Fatigue of hydrogels. Eur. J. Mech. A/Solids 74, 337–370. https://doi.org/10.1016/j.euromechsol.2018.12.001

Ciavarella, M., Cricri, G., McMeeking, R., 2021. A comparison of crack propagation theories in viscoelastic materials. Theor. Appl. Fract. Mech. 116, 103113. https://doi.org/10.1016/j.tafmec.2021.103113

Creton, C., 2003. Pressure-sensitive adhesives: An introductory course. MRS Bull. 28, 434–439. https://doi.org/10.1557/mrs2003.124

Creton, C., Ciccotti, M., 2016. Fracture and adhesion of soft materials: a review. Reports Prog. Phys. 79, 046601. https://doi.org/10.1088/0034-4885/79/4/046601

de Gennes, P.G., 1996. Soft adhesives. Langmuir 12, 4497–4500. https://doi.org/10.1021/la950886y

Deng, B., Wang, S., Hartquist, C., Zhao, X., 2023. Nonlocal Intrinsic Fracture Energy of Polymerlike Networks. Phys. Rev. Lett. 131, 228102. https://doi.org/10.1103/PhysRevLett.131.228102

Diani, J., Fayolle, B., Gilormini, P., 2009. A review on the Mullins effect. Eur. Polym. J. 45, 601–612. https://doi.org/10.1016/j.eurpolymj.2008.11.017

Ducrot, E., Chen, Y., Bulters, M., Sijbesma, R.P., Creton, C., 2014. Toughening elastomers with sacrificial bonds and watching them break. Science 344, 186–189. https://doi.org/10.1126/science.1248494

Feng, X., Hall, M.S., Wu, M., Hui, C.Y., 2014. An adaptive algorithm for tracking 3D bead displacements: Application in biological experiments. Meas. Sci. Technol. 25, 55701. https://doi.org/10.1088/0957-0233/25/5/055701

Gent, A.N., 1996. Adhesion and strength of viscoelastic solids. Is there a relationship between adhesion and bulk properties? Langmuir 12, 4492–4495. https://doi.org/10.1021/la950887q

Gong, J.P., 2010. Why are double network hydrogels so tough? Soft Matter 6, 2583–2590. https://doi.org/10.1039/b924290b

Gong, J.P., Katsuyama, Y., Kurokawa, T., Osada, Y., 2003. Double-network hydrogels with extremely high mechanical strength. Adv. Mater. 15, 1155–1158. https://doi.org/10.1002/adma.200304907

Graham, G.A.C., 1968. The correspondence principle of linear viscoelasticity theory for mixed boundary value problems involving time-dependent boundary regions. Q. Appl. Math. 26, 167–174. https://doi.org/10.1090/qam/99860

Greensmith, H.W., 1964. Rupture of rubber. XI. Tensile rupture and crack growth in a noncrystallizing rubber. J. Appl. Polym. Sci. 8, 1113–1128. https://doi.org/10.1002/app.1964.070080308

Greenwood, J.A., 2004. The theory of viscoelastic crack propagation and healing. J. Phys. D. Appl. Phys. 37, 2557–2569. https://doi.org/10.1088/0022-3727/37/18/011

Holzapfel, G.A., 2002. Nonlinear solid mechanics: a continuum approach for engineering science. Meccanica 37, 489–490. https://doi.org/10.1023/A:1020843529530

Hui, C.Y., Xu, D. Ben, Kramer, E.J., 1992. A fracture model for a weak interface in a viscoelastic material (small scale yielding analysis). J. Appl. Phys. 72, 3294–3304. https://doi.org/10.1063/1.351451

Hui, C.Y., Zhu, B., Long, R., 2022. Steady state crack growth in viscoelastic solids: A comparative study. J. Mech. Phys. Solids 159, 104748. https://doi.org/10.1016/j.jmps.2021.104748

Ju, J., Sanoja, G.E., Nagazi, M.Y., Cipelletti, L., Liu, Z., Hui, C.Y., Ciccotti, M., Narita, T., Creton, C., 2023. Real-Time Early Detection of Crack Propagation Precursors in Delayed Fracture of Soft Elastomers. Phys. Rev. X 13, 021030. https://doi.org/10.1103/PhysRevX.13.021030

Kim, J., Zhang, G., Shi, M., Suo, Z., 2021. Fracture, fatigue, and friction of polymers in which entanglements greatly outnumber cross-links. Science 374, 212–216. https://doi.org/10.1126/science.abg6320

Knauss, W.G., 2015. A review of fracture in viscoelastic materials. Int. J. Fract. 196, 99–146. https://doi.org/10.1007/s10704-015-0058-6

Knauss, W.G., 1973. On the steady propagation of a crack in a viscoelastic sheet: experiments and analysis, in: Kausch, H.H., Hassell, J.A., Jaffee, R.I. (Eds.), Deformation and Fracture of High Polymers. Springer US, pp. 501–541. https://doi.org/10.1007/978-1-4757-1263-6_27

Lake, G.J., Thomas, A.G., 1967. The strength of highly elastic materials. Proc. R. Soc. London. Ser. A. Math. Phys. Sci. 300, 108–119. https://doi.org/10.1098/rspa.1967.0160

Li, C., Wei, X., Wang, M., Adda-Bedia, M., Kolinski, J.M., 2023. Crack tip kinematics reveal the process zone structure in brittle hydrogel fracture. J. Mech. Phys. Solids 178, 105330. https://doi.org/10.1016/j.jmps.2023.105330

Li, C., Yang, H., Suo, Z., Tang, J., 2020. Fatigue-Resistant elastomers. J. Mech. Phys. Solids 134, 103751. https://doi.org/10.1016/j.jmps.2019.103751

Lin, S., Liu, J., Liu, X., Zhao, X., 2019a. Muscle-like fatigue-resistant hydrogels by mechanical training. Proc. Natl. Acad. Sci. U. S. A. 116, 10244–10249. https://doi.org/10.1073/pnas.1903019116

Lin, S., Liu, X., Liu, J., Yuk, H., Loh, H.C., Parada, G.A., Settens, C., Song, J., Masic, A., McKinley, G.H., Zhao, X., 2019b. Anti-fatigue-fracture hydrogels. Sci. Adv. 5, eaau8528. https://doi.org/10.1126/sciadv.aau8528

Lin, S., Londono, C.D., Zheng, D., Zhao, X., 2022. An extreme toughening mechanism for soft materials. Soft Matter 18, 5742–5749. https://doi.org/10.1039/D2SM00609J

Liu, W., Long, R., 2016. Constructing continuous strain and stress fields from spatially discrete displacement data in soft materials. J. Appl. Mech. Trans. ASME 83, 011006. https://doi.org/10.1115/1.4031763

Long, R., Hui, C.Y., 2016. Fracture toughness of hydrogels: Measurement and interpretation. Soft Matter 12, 8069–8086. https://doi.org/10.1039/c6sm01694d

Lu, Y., Qi, Y., Tenardi, M., Long, R., 2021. Mixed-mode fracture in a soft elastomer. Extrem. Mech. Lett. 48, 101380. https://doi.org/10.1016/j.eml.2021.101380

Nian, G., Kim, J., Bao, X., Suo, Z., 2022. Making Highly Elastic and Tough Hydrogels from Doughs. Adv. Mater. 34, 2206577. https://doi.org/10.1002/adma.202206577

Persson, B.N.J., Brener, E.A., 2005. Crack propagation in viscoelastic solids. Phys. Rev. E 71, 036123. https://doi.org/10.1103/PhysRevE.71.036123

Qi, Y., Caillard, J., Long, R., 2018. Fracture toughness of soft materials with rate-independent hysteresis. J. Mech. Phys. Solids 118, 341–364. https://doi.org/10.1016/j.jmps.2018.05.020

Qi, Y., Li, X., Venkata, S.P., Yang, X., Sun, T.L., Hui, C.-Y., Gong, J.P., Long, R., 2024. Mapping deformation and dissipation during fracture of soft viscoelastic solid. J. Mech. Phys. Solids 186, 105595. https://doi.org/10.1016/j.jmps.2024.105595

Qi, Y., Zou, Z., Xiao, J., Long, R., 2019. Mapping the nonlinear crack tip deformation field in soft elastomer with a particle tracking method. J. Mech. Phys. Solids 125, 326–346. https://doi.org/10.1016/j.jmps.2018.12.018

Roucou, D., Diani, J., Brieu, M., Colombo, D., 2020. Experimental identification of fracture toughness of a carbon black-filled styrene butadiene rubber undergoing energy dissipation by Mullins softening. Mech. Mater. 151, 103645. https://doi.org/10.1016/j.mechmat.2020.103645

Roucou, D., Diani, J., Brieu, M., Mbiakop-Ngassa, A., 2019. Critical strain energy release rate for rubbers: single edge notch tension versus pure shear tests. Int. J. Fract. 216, 31–39. https://doi.org/10.1007/s10704-018-00336-8

Saulnier, F., Ondarçuhu, T., Aradian, A., Raphaël, E., 2004. Adhesion between a viscoelastic material and a solid surface. Macromolecules 37, 1067–1075. https://doi.org/10.1021/ma021759t

Schapery, R.A., 1975a. A theory of crack initiation and growth in viscoelastic media - I. Theoretical development. Int. J. Fract. 11, 141–159. https://doi.org/10.1007/BF00034721

Schapery, R.A., 1975b. A theory of crack initiation and growth in viscoelastic media II. Approximate methods of analysis. Int. J. Fract. 11, 369–388. https://doi.org/10.1007/BF00033526

Schapery, R.A., 1975c. A theory of crack initiation and growth in viscoelastic media - III. Analysis of continuous growth. Int. J. Fract. 11, 549–562. https://doi.org/10.1007/BF00116363

Simo, J.C., 1987. On a fully three-dimensional finite-strain viscoelastic damage model: Formulation and computational aspects. Comput. Methods Appl. Mech. Eng. 60, 153–173. https://doi.org/10.1016/0045-7825(87)90107-1

Slootman, J., Waltz, V., Yeh, C.J., Baumann, C., Göstl, R., Comtet, J., Creton, C., 2020. Quantifying rate-and temperature-dependent molecular damage in elastomer fracture. Phys. Rev. X 10, 041045. https://doi.org/10.1103/PhysRevX.10.041045

Sun, J.Y., Zhao, X., Illeperuma, W.R.K., Chaudhuri, O., Oh, K.H., Mooney, D.J., Vlassak, J.J., Suo, Z., 2012. Highly stretchable and tough hydrogels. Nature 489, 133–136. https://doi.org/10.1038/nature11409

Tang, J., Li, J., Vlassak, J.J., Suo, Z., 2017. Fatigue fracture of hydrogels. Extrem. Mech. Lett. 10, 24–31. https://doi.org/10.1016/j.eml.2016.09.010

Tsunoda, K., Busfield, J.J.C., Davies, C.K.L., Thomas, A.G., 2000. Effect of materials variables on the tear behaviour of a non-crystallizing elastomer. J. Mater. Sci. 35, 5187–5198. https://doi.org/10.1023/A:1004860522186

Vernerey, F.J., Long, R., Brighenti, R., 2017. A statistically-based continuum theory for polymers with transient networks. J. Mech. Phys. Solids 107, 1–20. https://doi.org/10.1016/j.jmps.2017.05.016

Wang, Z., Xiang, C., Yao, X., Le Floch, P., Mendez, J., Suo, Z., 2019. Stretchable materials of high toughness and low hysteresis. Proc. Natl. Acad. Sci. U. S. A. 116, 5967–5972. https://doi.org/10.1073/pnas.1821420116

Wang, Z., Zheng, X., Ouchi, T., Kouznetsova, T.B., Beech, H.K., Av-Ron, S., Matsuda, T., Bowser, B.H., Wang, S., Johnson, J.A., Kalow, J.A., Olsen, B.D., Gong, J.P., Rubinstein, M., Craig, S.L., 2021. Toughening hydrogels through force-triggered chemical reactions that lengthen polymer strands. Science 374, 193. https://doi.org/10.1126/science.abg2689

Xiang, C., Wang, Z., Yang, C., Yao, X., Wang, Y., Suo, Z., 2019. Stretchable and fatigue-resistant materials. Mater. Today. https://doi.org/10.1016/j.mattod.2019.08.009

Yang, C., Yin, T., Suo, Z., 2019. Polyacrylamide hydrogels. I. Network imperfection. J. Mech. Phys. Solids 131, 43–55. https://doi.org/10.1016/j.jmps.2019.06.018

Zhang, T., Lin, S., Yuk, H., Zhao, X., 2015. Predicting fracture energies and crack-tip fields of soft tough materials. Extrem. Mech. Lett. 4, 1–8. https://doi.org/10.1016/j.eml.2015.07.007

Zhao, X., 2014. Multi-scale multi-mechanism design of tough hydrogels: building dissipation into stretchy networks. Soft Matter 10, 672–87. https://doi.org/10.1039/c3sm52272e